
Spectral wave modelling of the extreme 2013/2014 winter storms in the North-East Atlantic

Ruju Andrea ^{1,4,*}, Filipot Jean-Francois ¹, Bentamy Abderrahim ², Leckler Fabien ^{1,3}

¹ France Energies Marines, Batiment Cap Ocean, Technopole Brest Iroise, F-29280 Plouzane, France.

² Inst Francais Rech & Exploitat Mer, Lab Oceanog Spatiale, F-29280 Plouzane, France.

³ Serv Hydrograph & Oceanog Marine, F-29200 Brest, France.

⁴ Univ Cagliari, Dept Chem & Geol Sci, I-09042 Monserrato, Italy.

* Corresponding author : Andrea Ruju, email address : rujua@unica.it

Abstract :

This work aims to investigate the impact of wind forcing datasets and wave breaking parameterizations on spectral wave model performance under extremely energetic conditions. For this purpose we used the wave model WaveWatch III to simulate the evolution of the highly energetic storms that occurred in winter 2013/2014 in the North-East Atlantic. We forced the wave model with two different wind datasets: one proceeding from the ECMWF ERAS reanalysis dataset and the other from satellite observations. Moreover, two wave energy dissipation parameterizations were tested: Test471 and Test500. The model accuracy was assessed by comparing the output datasets with buoy data both in deep and coastal water. Moreover, wave height measurements from satellite were used to assess the model accuracy along storm tracks across the ocean. The accuracy of simulated results shows a significant dependence on the wind forcing and wave dissipation parameterization used. Error metrics computed under storm conditions at wave buoys are consistent with those computed along storm tracks. At the wave buoy locations, all datasets tend to underestimate wave parameters at the peaks of the storms.

Highlights

► The choice of the breaking parameterization and the wind forcing affects the performance of WaveWatch III under storms. ► The error metrics computed under storm conditions at wave buoys are consistent with those computed along storm tracks. ► A significant underestimation of extreme wave conditions at the storm peak is found. ► The high-resolution wind forcing ERA5 does not significantly improve the error statistics computed at the wave buoys.

Keywords : Spectral wave modelling, Wind forcing, Wave energy dissipation, Wave breaking, Extreme storms, Storm tracking

1. Introduction

Recent work has reported that extreme sea state conditions have increased in terms of frequency and intensity in the last decades (Young and Ribal, 2019; Reguero et al., 2018). This trend, related to climate change and possibly involved in a long-term tendency, has significance for engineering applications: among them we can mention coastal hazard assessment, offshore ship operations and the design of marine structures. Marine engineers and scientists often combine datasets proceeding from different sources in an effort to achieve an accurate and exhaustive description of extreme events and their impacts (O'Reilly et al., 2016; Castelle et al., 2015; Masselink et al., 2016). In this context, by integrating in situ and remote measurements, third-generation spectral wave models and their output make a fundamental contribution towards a better understanding and prediction of extreme wave events.

Third-generation spectral wave models are widely used nowadays for wave hindcast and forecast at global and regional scales (Bernier et al., 2016; Besio et al., 2016; Perez et al., 2017; Sandhya et al., 2018; Ruju et al., 2019). These models solve the wave action balance equation with a set of source terms encompassing the effects of physical processes from wave generation to dissipation (Tolman et al., 2013). Although the recent implementation of physical-based parameterizations has led to an increase of model output accuracy, simulating extreme wave events remains a challenge (van Vledder et al., 2016; Holthuijsen et al., 2012; Zieger et al., 2015; Campos et al., 2019). This is mainly due the paucity of observations available during the evolution and at the peak of extreme events with respect to moderate and more frequent conditions. As a result of the data used during the parameterization development and model calibration processes, model uncertainties are generally higher for rare wave conditions. For instance, Filipot and Ardhuin (2012) reported a deterioration of error statistics associated with different parameterizations for significant wave heights above 8 m.

Under energetic and storm conditions characterized by large wave steepness values, the wave energy dissipation parameterization takes a key role in spectral evolution and wave growth limitation. Despite the significant attention received, it is likely to represent the least understood source term (Ardhuin et al., 2010). In addition to parameterizations, it is well acknowl-

36 edged that wave model accuracy strongly depends on the accuracy of the
37 wind forcing dataset (Stopa et al., 2016). This work aims to investigate
38 the impact of two different wave breaking parameterizations and two wind
39 forcing dataset under extremely energetic wave conditions. We use the third
40 generation wave model WaveWatchIII (WWIII), version 5.16, to simulate the
41 sequence of severe storms occurred that in the North-East Atlantic during the
42 winter 2013/2014.

43 Previous work has recognized the winter of 2013/2014 as one of the most
44 exceptional in terms of storm sequence and intensity in the North-East At-
45 lantic Ocean (Wadey et al., 2014; Masselink et al., 2016). Due to the rela-
46 tively south paths of these extra-tropical cyclones, extreme energetic wave
47 conditions were recorded by coastal monitoring systems of Western European
48 countries, from Portugal to Ireland. On coastal areas, these storms drove
49 extreme surge, runup and overtopping causing large morphological changes
50 and strong damage to infrastructures (Castelle et al., 2015; Scott et al., 2016;
51 Autret et al., 2016).

52 The two wave energy dissipation parameterizations tested in this work are
53 Test471 and 500. They are both included in the parameterization group ST4
54 available in WWIII version 5.16. Moreover, we assess the impact of two wind
55 forcing datasets. One of them is constituted by the wind analysis obtained
56 through the use of various remotely sensed wind observations (Bentamy et al.,
57 2019; Desbiolles et al., 2017). The other is the ERA5 reanalysis dataset
58 (Hersbach et al., 2019). Model accuracy is assessed by comparing simulated
59 results with the measurements from buoys located in the North-East Atlantic
60 as well as satellite observations along storm tracks.

61 **2. Methods**

62 *2.1. Data collection and storm identification at wave buoys*

63 We collected in situ wave parameters from eight North-East Atlantic wave
64 buoys belonging to different observational networks. Two of them (62163 and
65 62001) are offshore buoys, located in water depths exceeding 2500 m. The
66 other six (62069, 62103, 62064, 4403, 5602, DW5) are coastal buoys deployed
67 in mean water depths ranging from 30 to 68 m (see Figure 1 showing the
68 geographical setting). Table 1 lists the wave buoys with mean water depth
69 and main wave parameters.

70 These buoys are exposed to a combination of long-period Atlantic swells
71 and locally-generated wind waves. Due to the shelter offered by the sur-

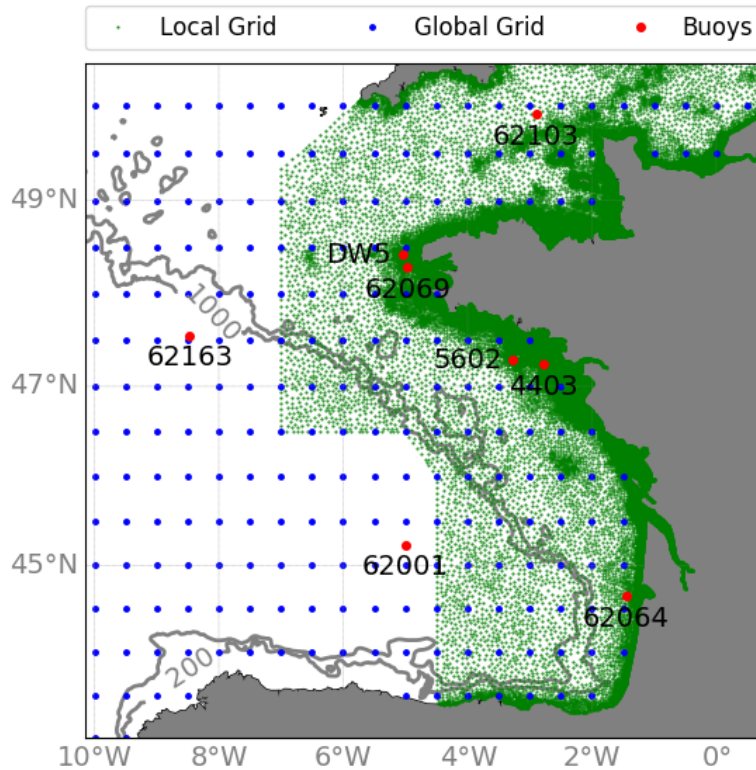


Figure 1: Global (blue dots) and local (green dots) grid configuration over the Eastern Atlantic region. Red dots indicate the buoy locations.

72 rounding coastline and small islands and the dissipation on the continental
 73 shelf, wave height at buoys 62103, 4403 and DW5 is significantly smaller
 74 than that at other locations. Buoy 62103 lies in the British channel and it
 75 is thus partially sheltered by the Brittany and Cornwall peninsulas. On the
 76 other hand, the presence of the islands of Ushant and Belle-Ile dampens the
 77 incoming wave energy hitting buoys DW5 and 4403, respectively. Wave prop-
 78 agation at coastal buoy locations is affected not only by topographic features
 79 but also by tidal dynamics (currents and water levels) that can be particu-
 80 larly intense in proximity of Brittany shores. All the buoys chosen in this
 81 work provide a high time coverage of nearly 100% for the winter 2013/2014
 82 on which this work focuses on.

Table 1: Wave buoys with mean water depth and significant wave height H_s statistics. for the period considered.

Buoy	depth [m]	mean H_s [m]	$H_{s,99}$ [m]	$H_{s,70}$ [m]
62163	2526	5.0	11.9	5.9
62001	4554	4.5	10.9	5.4
62069	66	3.9	9.6	4.7
62103	68	2.6	7.1	3.1
62064	54	3.4	8.2	4.1
4403	30	2.4	5.8	3.0
5602	45	3.6	8.7	4.3
DW5	42	2.5	6.6	3.0

83 We used the peak-over-threshold (POT) (Mathiesen et al., 1994) method
84 to identify the 24-hour independent storms occurred during the 2013/2014
85 winter at buoy 62163. The H_s threshold was chosen equal to the 30% ex-
86 ceedance H_s ($H_{s,70}$) calculated over the 2013/2014 winter period. We retained
87 only the storms with a duration larger than 12 h that met the independence
88 criterium with more than 24 hours between the end of a storm and the be-
89 ginning of the following one. Although the threshold value of 30% may seem
90 low for extreme event analysis, due to the highly-energetic period consid-
91 ered, this method allowed the identification of 13 storms in the winter period
92 comprised between the 21th of December and the 21th of March (dates usu-
93 ally taken as of the meteorological start and end of winter). However, we
94 extended the winter period up to the 31 of March to include the 14th storm
95 occurred on the 24th of March; see upper panel of Figure 2. The extreme
96 wave parameters representative of each storm of the sample were selected
97 as the values occurring at the time in which the maximum wave height was
98 observed during the storm duration.

99 The adoption of the same method, used for the event identification at
100 buoy 62163, would have led to a different number of storms at each buoy
101 location. For consistency, we recognized at buoys locations the same storms
102 first identified at the offshore buoy 62163. Since this buoy lies at the western-
103 most location and North-East Atlantic storms are mainly moving eastward
104 (Dodet et al., 2010), they are likely to hit first buoy 62163 and then continue
105 propagating until they reach the other buoys. For this reason, at the other

106 buoy location we expect that both the beginning and the end of a storm
107 happen later than at buoy 62163. Therefore, we identified the beginning of
108 a storm at each buoy location as the time at which H_s firstly increases over
109 $H_{s,70}$ after the beginning of the storm at 62163. Analogously, the end of the
110 storm was set at the time at which H_s falls below $H_{s,70}$ after the end of the
111 storm at 62163. Note that $H_{s,70}$ is different at each location.

112 The criteria of storm independence and minimal duration prescribed at
113 buoy 62163 are not always met at the other locations. This is particularly
114 evident at buoy 4403 where, just before the February 10th, storms S7 and
115 S8 are contiguous since H_s remains above the threshold for a considerable
116 amount of time from the start of storm S7 to the end of the storm S8. Nev-
117 ertheless, this procedure has the main benefit of allowing the identification
118 of the same storms (14 in number) at each buoy location, each of them being
119 related to the same synoptic system (see Figure 2 that highlights the storms
120 over the time series of H_s measured by buoys).

121 *2.2. Data collection and storm tracking from atmospheric pressure*

122 We used the fifth generation ECMWF atmospheric reanalysis ERA5 (Hers-
123 bach et al., 2019) as a database to track the low-pressure systems propagation
124 across the Atlantic Ocean during the 2013/2014 winter. We identified the
125 low-pressure systems from the atmospheric pressure at the sea level. First, at
126 each ERA5 output time instant the active low-pressure systems (that we can
127 classify as extra-tropical cyclones) were identified as those systems that have
128 a pressure value lower than 980 hPA and imposing a minimum distance of 5°
129 between different systems. Moreover, the evolution of system propagation in
130 time and space was made assuming a maximum velocity of 120 km/h (33.3
131 m/s) of the low-pressure system.

132 This method led to the identification of a large number of low-pressure
133 systems whose life duration spanned from few hours up to several days for
134 the most persistent. To focus on the same events recognized at the buoy
135 locations, we looked for the active systems at the time arrival of the 14
136 energetic storms, in terms of H_s , recorded at the buoy 62163. We named
137 these low-pressure systems with the same name of the storms they drove
138 at the buoy locations (S1, S2, etc.). Since an energetic low-pressure system
139 drove the H_s peak occurred in the last stage of storm S4 at buoy 62163, we
140 added this one (calling it S4B) to the sample constituted by the 14 systems
141 that were active at the beginning of the 14 storms. Once identified, the
142 propagation path of these 15 systems, responsible for the largest wave heights

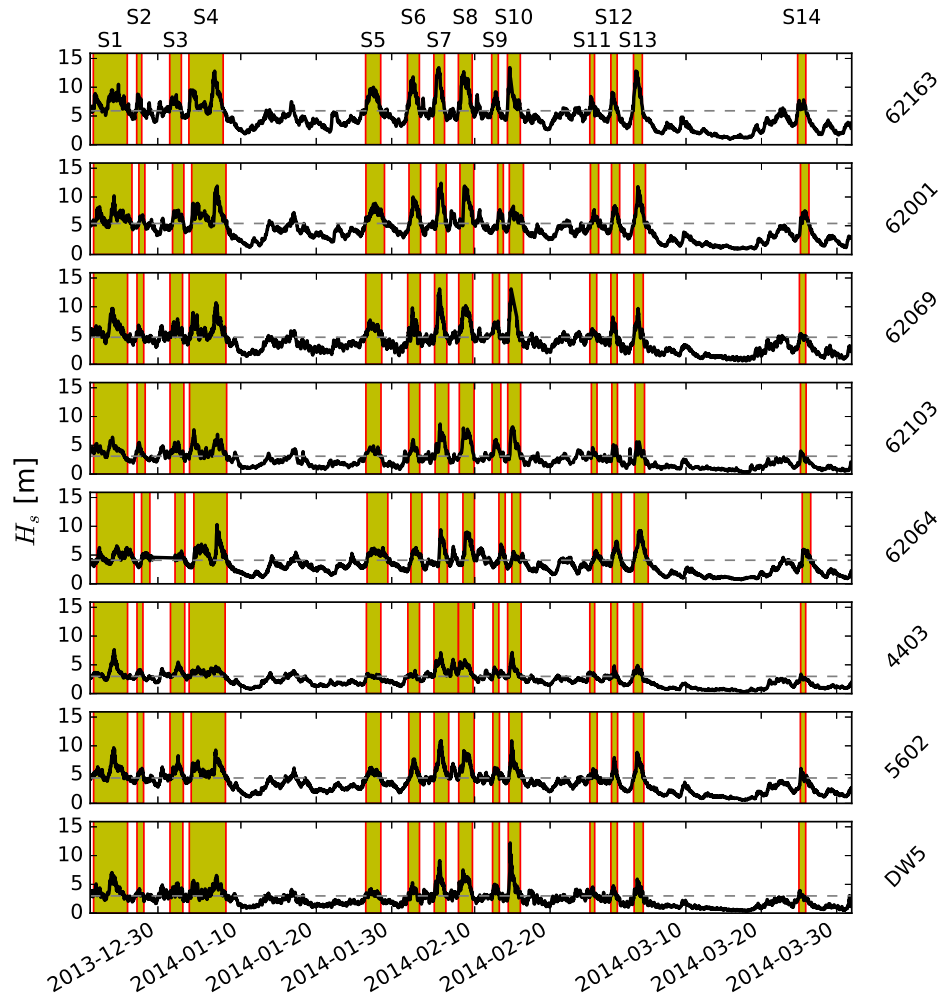


Figure 2: Time series of significant wave height H_s at the buoy locations. Yellow rectangles extend over the storm duration. Grey dashed lines indicate the H_s thresholds $H_{s,70}$ used for storm identification.

143 in the winter 2013/2014, was tracked back from its generation in the Western
 144 Atlantic and forward to its dissolution in the Eastern Atlantic. Figure 3 shows
 145 the paths of the low-pressure systems highlighting the intense extra-tropical
 146 cyclones driving the the five highest H_s at the storm peak at buoy 62163.

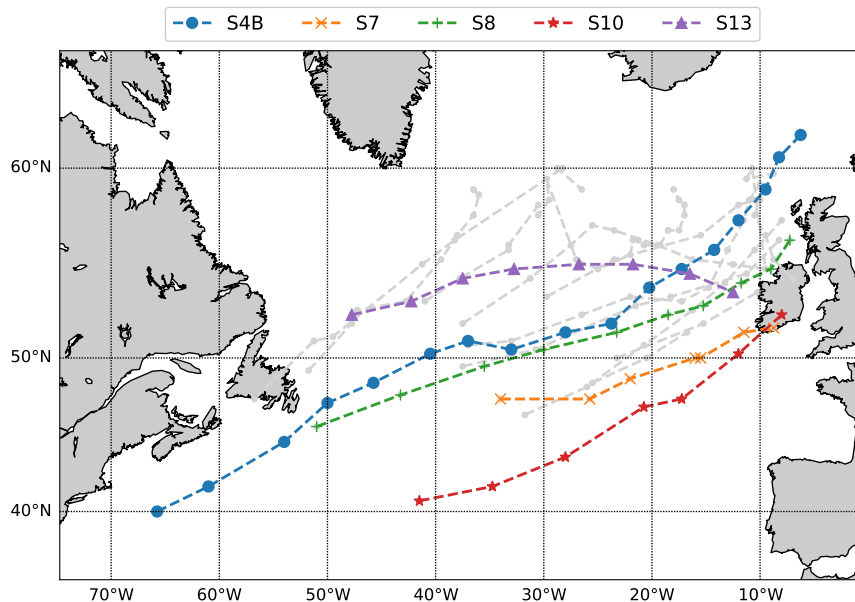


Figure 3: Paths of the low-pressure systems recorded in the winter 2013/2014 in the North Atlantic. The paths of the 5 most intense systems are highlighted by coloured lines. Markers are 6-hour spaced.

147 *2.3. Modelling techniques*

148 We used the numerical model WAVEWATCH III (WWIII) (Tolman,
 149 2016) version 5.16 to simulate the energetic wave dynamics that occurred in
 150 the winter 2013/2014. WWIII is a spectral wave model able to reproduce the
 151 physical processes governing wave motion over a wide range of water depths.
 152 Its physical and numerical configurations make it suitable to perform hind-
 153 cast and forecast at global and regional scales. The governing equation of
 154 the model is the wave action balance equation in which the source and sink

155 of wave energy is taken into account by means of a set of source terms:

$$156 \quad \frac{DN}{Dt} = \frac{S}{\sigma}, \quad (1)$$

157 where D/Dt represents the total derivative (moving with a wave component)
158 and S represents the net effect of sources and sinks for the wave action
159 spectrum $N = E/\sigma$ (where E is the energy spectrum and σ is the intrinsic
160 frequency of the wave). Parameterizations are usually divided into four main
161 source terms: atmospheric S_{atm} , nonlinear S_{nl} , ocean S_{oc} and bottom S_{bt} .
162 This work focuses on the parameterization of wave energy dissipation by
163 breaking included in the ocean term S_{oc} , that is assumed to be the most
164 important sink of wave energy in storm seas (van Vledder et al., 2016).

165 In this study, a multigrid approach allowed the optimization of compu-
166 tational cost given the wide range of physical process scales we are focusing
167 on: from the long scales of wave and swell generation in the deep ocean
168 to the small scales of wave-current interaction and depth-induced processes
169 in coastal water. The model ran over a rectangular grid with a constant
170 spatial resolution of 0.5° covering the entire globe. Wave spectra computed
171 over this grid represented the boundary conditions for the coastal simula-
172 tions performed over an unstructured grid extending over coastal water from
173 Northern Spain in the South to the British channel in the North. This
174 unstructured mesh was developed in the scope of the HOMONIM project,
175 funded by the French government, in order to improve the operational wave
176 surge forecasting system along French Atlantic coast (Michaud et al., 2015).
177 It is made up of 92757 nodes with a decreasing resolution from 10 km at
178 offshore boundaries to about 200 m at the coastline and is supported by
179 an accurate and recent 100 m resolution bathymetry also developed in the
180 HOMONIM project (see Biscara et al. (2014)). The triangle-based grid is
181 used in WAVEWATCH III with the explicit N-scheme based on contour resid-
182 ual distribution (see Roland (2009) for a review). Initially implemented in
183 the Wind Wave Model-II (WWM-II), this numerical scheme have then been
184 successfully validated in WAVEWATCH III on an unstructured mesh closely
185 similar to ours (Ardhuin et al., 2009; Boudiere et al., 2013). See figure 1 that
186 shows the model grid configuration together with the location of the buoys.
187 It is worth mentioning that, the mean water depths of 4 coastal buoys given
188 in table 1 are between the minimum and maximum water depths extracted
189 from the model simulations, as expected. The exceptions are buoys 5602 and
190 4403 whose mean water depth provided by the responsible entity (CEREMA

191 in this case) is smaller than the depth ranges from the model: water depth
 192 ranges 56-61 m at 5602 and 35-41 m at 4403.

193 We discretized the WWIII wave spectra into 32 frequencies and 24 direc-
 194 tions. The frequency range extended from 0.0373 to 0.716 Hz, with a fre-
 195 quency increment factor of 1.1. Wave directions were linearly spaced resulting
 196 in an angular resolution of 15° . Resonant nonlinear wave-wave interactions
 197 occurring between four wave components (quadruplets) were computed with
 198 the Discrete Interaction Approximation (DIA) method. Triad wave interac-
 199 tions, accounting for nonlinear energy transfer in the nearshore, were also
 200 included through the LTA model. Wave dissipation was simulated with the
 201 parameterizations of Ardhuin et al. (2010) and Filipot and Ardhuin (2012) in
 202 Test471 and Test500, respectively (see section 2.4). Table 2 lists the parame-
 203 terizations used for the main source terms, see the WWIII manual (Tolman,
 204 2016) for an exhaustive description of these terms. Note that both Test471
 205 and Test500 are included in parameterization group ST4.

Table 2: Source term treatment in WWIII.

	$S_{in} + S_{ds}$	S_{nl}	S_{tr}	S_{bot}	S_{db}	S_{bs}
Parameterization	ST4	NL1	TR1	BT4	DB1	BS1

206 2.4. Parameterization of the dissipation induced by wave breaking

207 The two wave dissipation parameterizations assessed in this work are
 208 those by Ardhuin et al. (2010) and Filipot and Ardhuin (2012). Consistent
 209 with previous literature (Filipot and Ardhuin, 2012; Leckler et al., 2013),
 210 they are referred to as Test471 and Test500, respectively. These formulations
 211 recognize that wave energy can be dissipated by the breaking process in
 212 two ways: a spontaneous breaking in which the energy of a wave packet
 213 is dissipated by the breaking of that very wave packet and a cumulative
 214 breaking dissipation in which energy dissipation is the result of the breaking
 215 of longer waves wiping out shorter waves. Test471 and Test500 differ in the
 216 way the spontaneous breaking source term S_{bk} is computed. For this reason
 217 we briefly outline here the computation process for S_{bk} .

218 2.4.1. Test471

219 Following the work of Phillips (1984), several wave parameterizations
 220 related breaking probability to spectral saturation. Ardhuin et al. (2010)
 221 (therein after ARD10) introduced a saturation-based semiempirical wave

222 breaking parameterization with a larger dissipation rate in the mean wave di-
 223 rection, consistent with the observations of Mironov and Dulov (2007). The
 224 directional saturation spectrum $B'(k, \theta)$ is defined as:

$$225 \quad B'(k, \theta) = \int_{\theta-\Delta}^{\theta+\Delta} k^3 \cos^2(\theta - \theta') E(k, \theta') d\theta', \quad (2)$$

226 with $\Delta=80^\circ$, $E(k, \theta')$ is the frequency spectrum and k is the wave number.
 227 ARD10 extrapolated the theory of Banner et al. (2000), originally formu-
 228 lated for dominant waves, over the entire directional spectrum to obtain the
 229 breaking probability parameterization Q_b :

$$230 \quad Q_b(k, \theta) = 28.16 \cdot \max[\sqrt{B'(k, \theta)} - \sqrt{B'_r}, 0]^2, \quad (3)$$

231 where B'_r is the breaking threshold with a correction providing a constant
 232 ratio of the root-mean-square orbital velocity and phase speed at different
 233 water depths d (Filipot et al., 2010):

$$234 \quad B'_r = B_r Y (M_4 Y^3 + M_3 Y^2 + M_2 Y + M_1), \quad (4)$$

235 where $Y = \tanh(kd)$. The deep water threshold B_r and the other constants
 236 in the polynomial fit can be found in ARD10. The factor 28.16 comes from
 237 the original factor of 22 of Banner et al. (2000), modified by taking into
 238 account that wave steepness is on the order of $1.6\sqrt{B'}$ and that the wave
 239 counting analysis for a given wave scale from Banner et al. (2000) tends to
 240 give a number of waves twice less than that expected for monochromatic
 241 waves. The dissipation term of spontaneous breaking S_{bk} is:

$$242 \quad S_{bk}(k, \theta) = \sigma \frac{C_{ds}}{B_r^2} \{ \delta_d \max[B(k) - B'_r, 0]^2 + (1 + \delta_d) \max[B'(k, \theta) - B'_r, 0]^2 \} E(k, \theta), \quad (5)$$

243 in which C_{ds} is a dissipation constant, δ_d is a coefficient that controls the
 244 directionality of breaking and $B(k)$ is the maximum value of $B'(k, \theta)$ for θ
 245 in the range $[0, 2\pi]$. Although this formulation is able to address both deep
 246 water and depth-induced breaking, ARD10 warned about the uncertainties
 247 involved in its application in shallow water environments.

248 *2.4.2. Test500*

249 With the main aim of overcoming the limitations of previous wave break-
 250 ing parameterizations, Filipot et al. (2010) and Filipot and Ardhuin (2012)

251 (therein after FAB12) made a significant effort towards a unified breaking
 252 parameterization valid from the deep ocean to the surf zone. Filipot et al.
 253 (2010) divided the frequency spectrum into wave scales with finite bandwidth
 254 centred at frequency f_i . Then, following Thornton and Guza (1983), they
 255 assumed that the breaking wave height distribution for each scale is given
 256 by the product of a Rayleigh distribution $P_R(H, f_i)$ and a weight function
 257 $W_b(H, f_i)$. In order to extend the formulation outside shallow water, they
 258 replaced the breaking criterion of Thornton and Guza (1983), based on the
 259 relative water depth H/d , with the breaking parameter defined by Miche
 260 (1944):

$$261 \quad \beta_r = \frac{\overline{k_r} H_r}{\tanh(\overline{k_r} d)}, \quad (6)$$

262 where $\overline{k_r}$ and H_r are the representative wave number and wave height for
 263 each wave scale f_i . The breaking wave height function W_b is:

$$264 \quad W_b(H, f_i) = 1.5 \left[\frac{\beta_r}{\beta_{t,lin}} \right]^2 \left\{ 1 - \exp \left[- \left(\frac{\beta}{\beta_{t,lin}} \right)^4 \right] \right\}, \quad (7)$$

265 where $\beta_{t,lin}$ is the breaking threshold defined by Miche (1944) but that takes
 266 into account the wave linearization (Filipot et al., 2010), inherent to the wave
 267 scale decomposition. The breaking probability for the wave scale with central
 268 frequency f_i is:

$$269 \quad Q_b(f_i) = \int_0^\infty P_R(H, f_i) \cdot W_b(H, f_i) dH. \quad (8)$$

270 The dissipation source term $S_{bk,i}$ for the component involved in the wave
 271 scale i is then given by:

$$272 \quad S_{bk,i}(f) = \frac{D(f_i) E(f)}{\int_0^\infty E(f) df}, \quad (9)$$

273 where $D(f_i)$ is the dissipation rate per unit area

$$274 \quad D(f_i) = Q_b(f_i) \Pi(f_i) \epsilon(f_i), \quad (10)$$

275 being $\Pi(f_i)$ and $\epsilon(f_i)$ the crest length density per unit area and the dissipation
 276 rate per unit length of breaking crest, respectively (Filipot and Ardhuin,
 277 2012).

278 Since the frequency windows overlap, each spectral component is asso-
279 ciated with several wave scales. The dissipation source term is expressed
280 as:

$$281 \quad S_{bk}(f) = \frac{1}{N} \sum_{i=1}^N S_{bk,i}(f), \quad (11)$$

282 in which N is the number of wave scales involving the frequency f .

283 *2.5. Atmospheric forcings*

284 In this work we tested the impact of two atmospheric forcing datasets on
285 WWIII model performance, under a winter characterized by a sequence of ex-
286 ceptionally energetic storm conditions in the North-East Atlantic (Masselink
287 et al., 2016). The first forcing dataset proceeds from the wind analysis ob-
288 tained through the use of various remotely sensed wind observations. On the
289 other hand, ERA5 reanalysis represents the second forcing dataset. These
290 forcing datasets are briefly described in the following sections.

291 Besides wind forcing, water levels and flow velocities computed by the
292 Model for Applications at Regional Scales (MARS) (Lazure and Dumas,
293 2008) were included in the WWIII simulations. MARS simulations were
294 carried out over three nested grids with spatial resolution ranging from 2 km
295 to 250 m in the shallower areas. MARS output was included only in the
296 simulations over the unstructured grid, allowing the computation of wave-
297 current interactions in the coastal environment.

298 *2.5.1. Satellite winds*

299 The remotely sensed data, also referred to as satellite wind analyses,
300 used in this study are mostly derived from scatterometer wind retrievals in
301 combination with radiometer observations (Bentamy et al., 2019; Desbiolles
302 et al., 2017). The main sources of remotely sensed wind data are from scat-
303 terometers onboard Metop-A (2007-present) and Metop-B (2012-present),
304 and named ASCAT-A and ASCAT-B. Ancillary remotely sensed data are de-
305 rived from radiometers Special Sensor Microwave Imager Sounder (SSMIS/S)
306 onboard the Defense Meteorological Satellite Program (DMSP) F16 (2003-
307 present) and F17 (2006-present), and from WindSat onboard Coriolis satellite
308 (2003-present).

309 The scatterometer retrieval in combination with radiometer wind ob-
310 servations, and with the European Center of Medium Weather Forecasts
311 (ECMWF) re-analysis model ERA Interim (Simmons et al., 2007), are used

312 for determining regular in space and time surface wind analyses (Desbiolles
313 et al., 2017). These are available at synoptic times (00h:00, 06h:00, 12h:00,
314 and 18h:00 UTC), over the global oceans with a spatial resolution of 0.25°
315 0.25° . Their accuracy, determined through comprehensive comparisons with
316 6-hourly averaged buoy winds, is of same order of scatterometer retrieval
317 accuracy.

318 Regarding the study topic, it is of interest to determine some statistics
319 aiming at the characterization of the remotely wind speed and direction anal-
320 yses at regional scale. To achieve such purpose, satellite wind analyses are
321 compared to collocated (in space and time) 6-hourly averaged wind speed
322 and direction measured by buoys 62103, 62163 and 62001 (see their location
323 in Figure 1). Scatter plots (not shown) indicate that satellite wind analyses
324 agree well with buoy estimates for all wind speed and direction ranges, in-
325 cluding high wind conditions. The correlation between buoy and satellite is
326 almost 1, while symmetrical regression slope and intercept parameter are 1
327 and of 0.1 m/s, respectively. Furthermore, the low Root Mean Square Error
328 RMSE values (lower than 1 m/s and 20° for wind speed and wind direction,
329 respectively) attest the quality of satellite wind analyses. Satellite data im-
330 prove the comparisons with insitu wind measurements with respect to the
331 ERA Interim model. In fact, the satellite wind dataset contributes to reduce
332 the bias and RMSE values, improving the comparisons for high wind condi-
333 tions and confirming the results of Bentamy et al. (2017) and Desbiolles
334 et al. (2017).

335 2.5.2. *ECMWF winds*

336 In 2018 ECMWF released the ERA5 reanalysis with spatial resolution
337 of 0.25° and 1-hour intervals (Hersbach et al., 2019). This dataset combines
338 worldwide observations with model data collected from the 1979 until present.
339 Atmospheric variables are given at the surface and on model levels. The
340 variables used as forcing for the WWIII simulations in this work are the
341 horizontal components of the wind speed at 10 m above the sea level (Tolman,
342 2016).

343 Although the ERA5 dataset was originally released with an hourly output
344 resolution, we reduced the time resolution to 6-hour intervals in the WWIII
345 forcing. This has been done with the purpose of having the two forcing
346 datasets assessed in this study with same spatial and time resolution, thus
347 ensuring an insightful result comparison. The influence of time resolution of
348 forcing winds on model results will be further addressed in section 4.

349 **3. Results**

350 The impact of forcing winds and energy dissipation parameterizations
 351 on model performance is assessed by comparing the simulated datasets with
 352 the datasets produced by buoy and altimeter observations. Here, we adopt
 353 normalized statistics with the main aim of comparing a large range of wave
 354 conditions. The normalized root-mean-square-error NRMSE and normalized
 355 bias NBIAS are defined as follows:

$$356 \quad \text{NRMSE} = \sqrt{\frac{\sum (O_i - M_i)^2}{\sum O_i^2}}. \quad (12)$$

$$357 \quad \text{NBIAS} = \frac{\sum (O_i - M_i)}{\sum O_i}. \quad (13)$$

358 where O_i and M_i are the observed and modelled variables.

359 For the sake of clarity we assign the names of each model output dataset
 360 by specifying the dissipation parameterization used followed by the wind
 361 forcing. For instance, the output including Test500 and the ECMWF forcing
 362 is called Test500ECMWF.

363 *3.1. Wave buoys*

364 Figure 4 shows the comparison between observed and modelled significant
 365 wave height H_s time series at the offshore buoy 62163 and at the coastal
 366 buoy 5602. Despite some differences among the four model outputs, overall
 367 the WWIII datasets are able to capture the main evolution of the observed
 368 dataset. However, evident discrepancies can be found at storm peaks where
 369 the modelled H_s underestimate the observations, especially in coastal water.
 370 An exception to this trend is represented by Test500Satellite at buoy 62163
 371 that seems to better represent the H_s evolution at the peak of the main
 372 storms.

373 To achieve a quantitative assessment of model performance, modelled
 374 time series are linearly interpolated over the observed time series. The scat-
 375 terplots of the total number of samples N , divided into deep water and
 376 coastal water, are shown in Figure 5, for the wave parameter H_s . NRMSE
 377 is on the order 0.1 at deep water buoy locations, ranging between 0.098
 378 for Test500ECMWF and 0.134 for Test500Satellite. Test500Satellite slightly
 379 overestimates H_s (NBIAS is 0.031), whereas a small underestimation is given

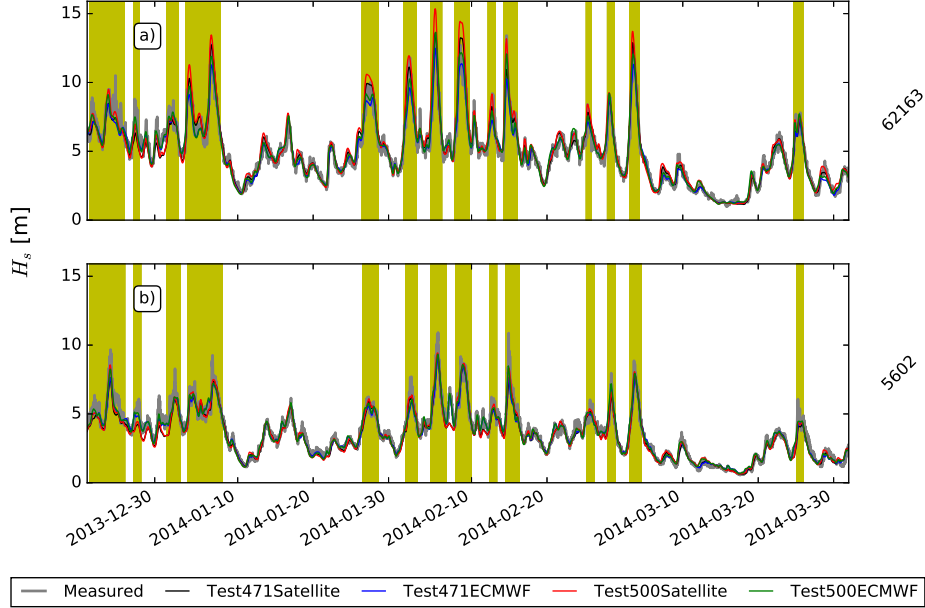


Figure 4: Observed (gray line) and predicted time series of significant wave height H_s at the deep water buoy 62163 (a) and at the coastal buoy 5602 (b). The four computed datasets are shown. Storms are coloured in yellow.

380 by Test471ECMWF (NBIAS is -0.025). The other two datasets are practi-
 381 cally unbiased ($|\text{NBIAS}| < 0.003$).

382 In general terms, for all datasets the NRMSE of H_s increases by few
 383 points percentage at coastal buoy locations. This is an expected result given
 384 the additional modelling challenges represented by the coastal environment
 385 (van Vledder et al., 2016), such as complex bathymetries and tidal currents,
 386 with respect to the deep ocean. A remarkable result comes from the obser-
 387 vation of coastal water scatterplots and the associated NBIAS of H_s . In fact,
 388 whereas all datasets overestimate H_s with positive NBIAS between 0.01 and
 389 0.042, the points associated to higher H_s ($H_s > 10\text{m}$) fall below the line of
 390 perfect agreement, meaning that those large H_s are underestimated. This is
 391 in agreement with the H_s underestimation at storm peaks already observed
 392 in Figure 4.

393 The analysis of model accuracy is integrated by the Taylor diagrams in

394 figure 6. All datasets have Correlation Coefficients larger than 0.95. In
395 deep water, Test471Satellite and Test500ECMWF have the larger agreement
396 with the observations in terms of Standard Deviation and RMSD. In coastal
397 water, the differences between datasets are less marked, with Test500Satellite
398 slightly improving the prediction in terms of Standard Deviation.

399 3.1.1. Storm evolution and peaks

400 To explore in more detail the model performance in addressing extreme
401 H_s , Figure 7 provides the scatterplots of observed and modelled H_s at the
402 storm peak. In this case the number of samples N is simply given by the
403 product of the number of storms times the number of locations. For all
404 datasets the NRMSE increases in coastal water. Moreover, NBIAS is always
405 negative confirming the H_s underestimation at storm peaks. Both in deep
406 and coastal water, Test500Satellite gives the lowest NBIAS in absolute value
407 (the underestimation is less pronounced). Whereas the largest H_s underes-
408 timation (minimum NBIAS) is provided by Test471ECMWF.

409 In contrast with Figure 7, we do not observe a systematic negative NBIAS
410 for H_s in Figure 8. This Figure shows the scatterplots of observed and mod-
411 elled H_s collected during storms in deep water and at coastal buoy locations.
412 In coastal water, the positive NBIAS values of datasets involving the param-
413 eterization Test500 are likely to be driven by the large number of H_s data
414 below 6 m. However, underestimation is still noticeable for more energetic
415 conditions ($H_s > 6$ m). Figure 10 aims at pointing out the difference between
416 the identification of the extreme H_s at the peak of a storm (the circle, in
417 this case storm S10) and the identification of the H_s values collected during
418 a storm (the thick line). Note that the time instants at which extreme H_s
419 occurs for the observed and modelled dataset do not necessarily coincide. For
420 instance, with the ECMWF and satellite datasets, the modelled maximum
421 is slightly ahead and delayed, respectively.

422 The Taylor diagrams of figure 9 integrate the information provided by the
423 scatter plots of figure 8. Correlation Coefficients are on the order of 0.9 for
424 all datasets. In deep, Test500Satellite gives the largest Standard Deviations.
425 In coastal water, the low values of the modelled Standard Deviations seem
426 to confirm the peak underestimation already suggested by the scatterplots
427 of figure 8.

428 Figure 11 shows the extreme wave energy flux F_e computed at the peak of
429 the storm and during the storm occurrence in coastal water. The wave energy
430 flux F_e is calculated from linear theory, assuming a Rayleigh distribution

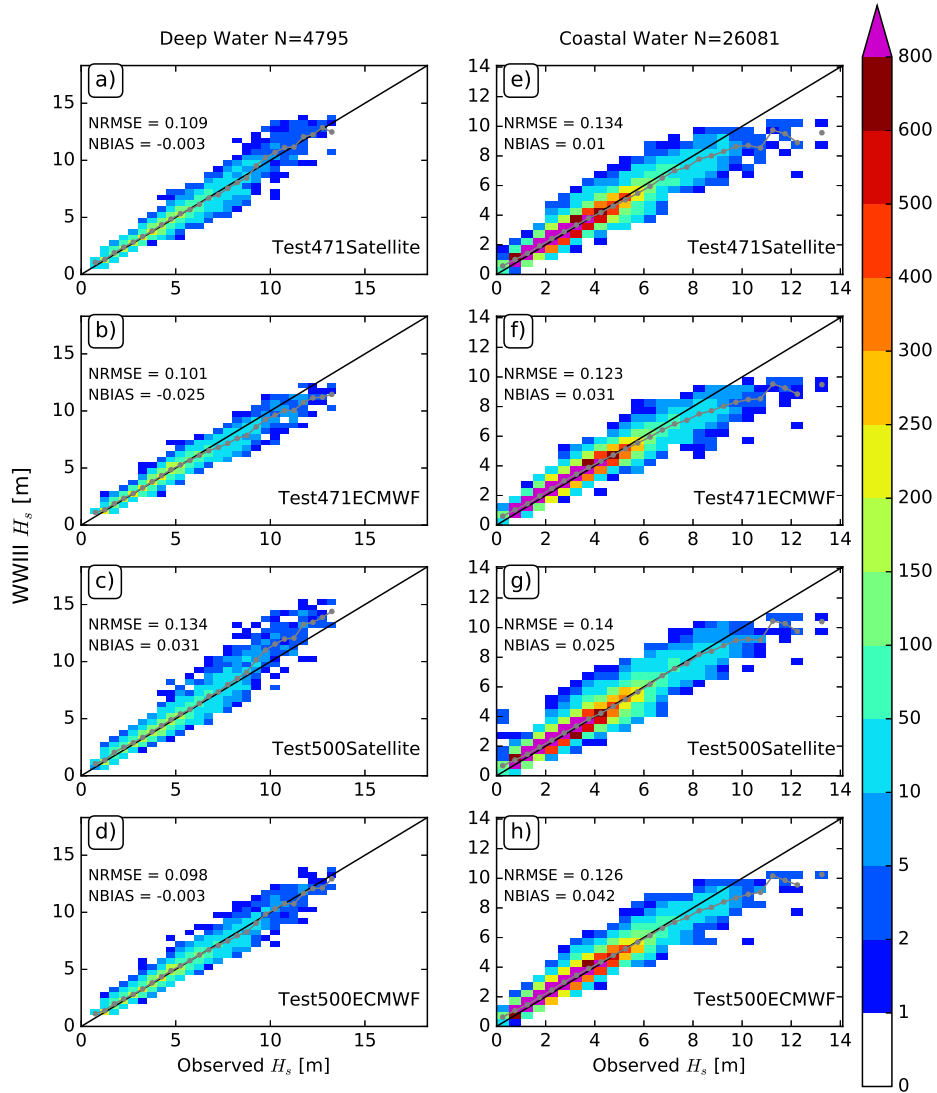


Figure 5: Scatter plot of observed versus modelled significant wave height H_s in deep water (a-d) and coastal water (e-h). The four datasets are shown. The grey line represents the mean of the model values.

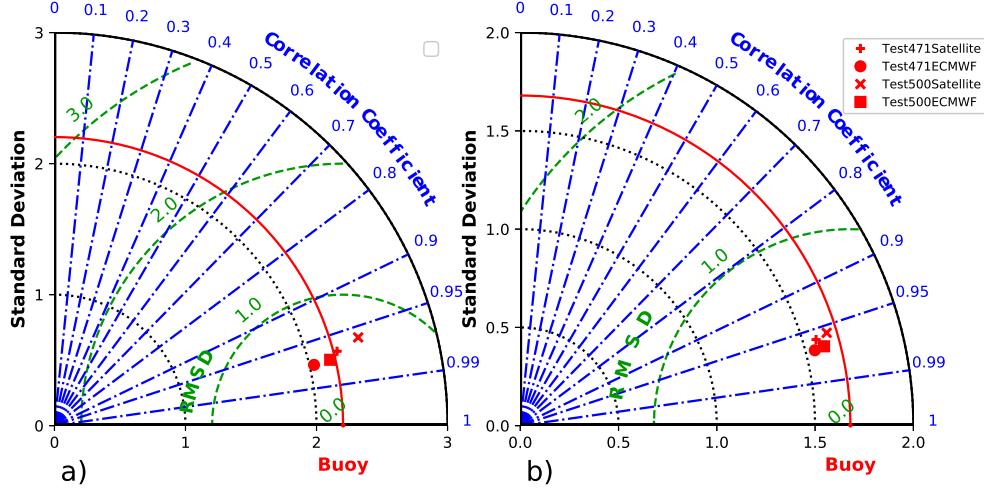


Figure 6: Taylor diagrams of Significant wave height in deep (a) and coastal (b) water.

431 of wave heights (Longuet-Higgins, 1952), as the product between the wave
 432 energy density E and the group celerity c_g :

$$F_e = E \cdot c_g, \quad (14)$$

433 in which

$$E = \frac{1}{8} \rho g H_{RMS}^2, \quad (15)$$

434

$$c_g = \frac{1}{2} c \left(1 + \frac{2kh}{\sinh(2kh)} \right), \quad (16)$$

435 where ρ is the water density, g is the acceleration of gravity, H_{RMS} is the
 436 root mean square wave height ($H_{RMS} = H_s/1.4$), c is the wave celerity, k
 437 is the wave number and h is the water depth. Both c and k are computed
 438 from linear wave theory using the mean period T_{02} . F_e plots tend to be
 439 more scattered than those of H_s , with Test471ECMWF providing the largest
 440 NRMSE for F_e both at the peak and during the storm. Test471ECMWF also
 441 gives the largest underestimation of F_e . Test500Satellite is the only dataset
 442 that overestimates F_e (NBIAS=0.05) during storms although, analogously
 443 the H_s trend commented in Figure 8, large values ($F_e > 0.5 \frac{MJ}{ms}$) are clearly
 444 underestimated. This point will be discussed in section 4. Tables 3 and 4
 445 list the error statistics of the four datasets at the wave buoys.

Table 3: H_s statistics.

H_s NRMSE						
Dataset	Deep Water			Coastal Water		
	All	Extreme	Storm	All	Extreme	Storm
T471Satellite	0.11	0.12	0.11	0.13	0.19	0.13
T471ECMWF	0.10	0.16	0.11	0.12	0.19	0.13
T500Satellite	0.13	0.09	0.14	0.14	0.16	0.14
T500ECMWF	0.10	0.11	0.10	0.13	0.16	0.13

H_s NBIAS						
Dataset	Deep Water			Coastal Water		
	All	Extreme	Storm	All	Extreme	Storm
T471Satellite	-0.00	-0.09	-0.01	0.01	-0.12	-0.00
T471ECMWF	-0.03	-0.15	-0.05	0.03	-0.13	0.00
T500Satellite	0.03	-0.01	0.05	0.03	-0.08	0.02
T500ECMWF	-0.00	-0.09	-0.01	0.04	-0.09	0.03

Table 4: T_2 and F_e statistics in coastal water.

Dataset	T_{02} NRMSE			F_e NRMSE		
	All	Extreme	Storm	All	Extreme	Storm
T471Satellite	0.12	0.11	0.08	0.33	0.51	0.34
T471ECMWF	0.09	0.14	0.08	0.34	0.55	0.36
T500Satellite	0.14	0.11	0.09	0.32	0.44	0.32
T500ECMWF	0.10	0.13	0.07	0.31	0.49	0.32

Dataset	T_{02} NBIAS			F_e NBIAS		
	All	Extreme	Storm	All	Extreme	Storm
T471Satellite	0.04	-0.05	0.01	-0.01	-0.35	-0.04
T471ECMWF	-0.01	-0.10	-0.03	-0.05	-0.42	-0.11
T500Satellite	0.06	-0.03	0.03	0.05	-0.27	0.05
T500ECMWF	0.00	-0.08	-0.02	-0.01	-0.36	-0.05

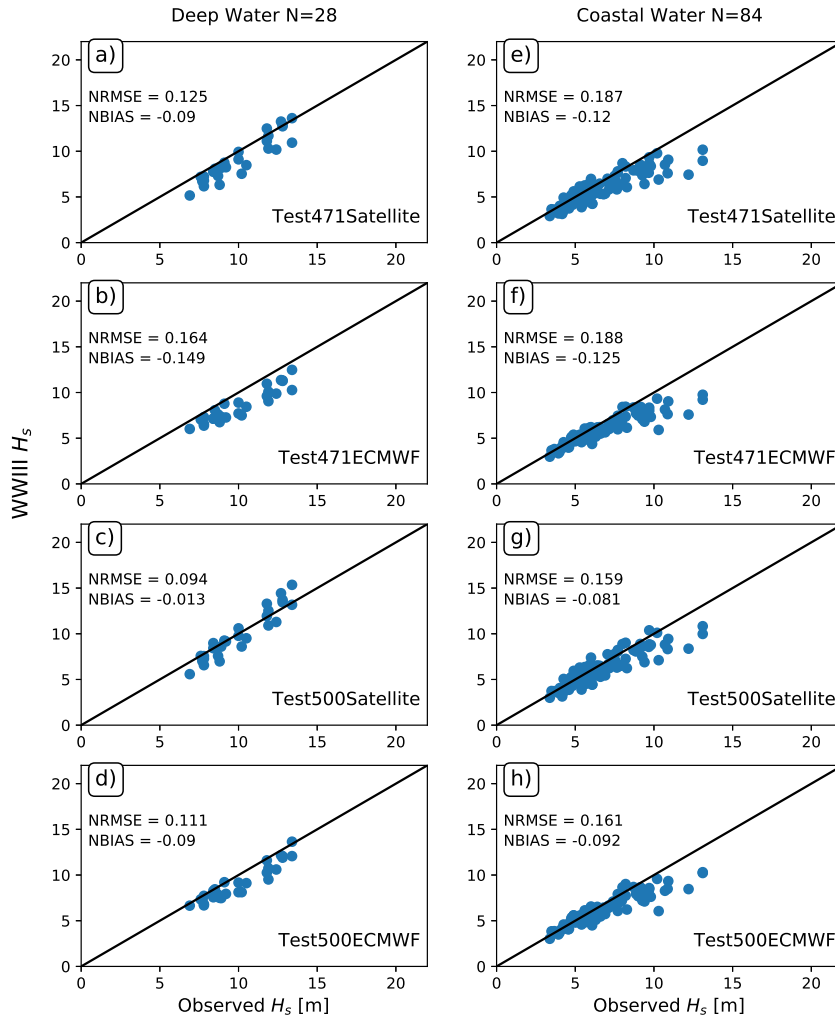


Figure 7: Scatter plot of observed versus modelled extreme significant wave height H_s in deep water (a-d) and coastal water (e-h). The four datasets are shown.

446 *3.1.2. Spectral wave analysis and sea/swell decomposition*

447 The availability of the two-dimensional spectra at the four coastal buoys
 448 managed by CEREMA (62069, 62064, 4403, 5602) allows the spectral anal-

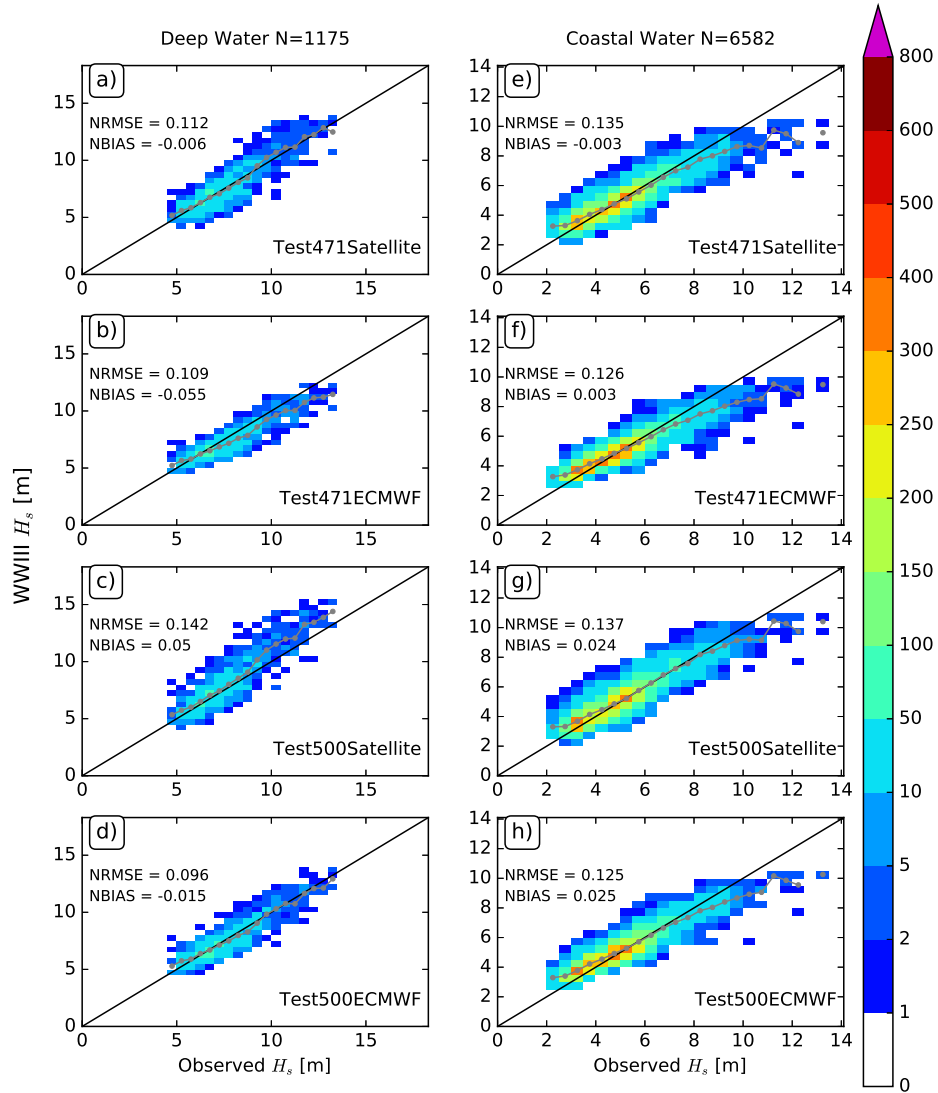


Figure 8: Scatter plot of observed versus modelled significant wave height H_s in deep water (a-d) and in coastal water (e-h) during storm duration. The four datasets are shown. The grey line represents the mean of the model values.

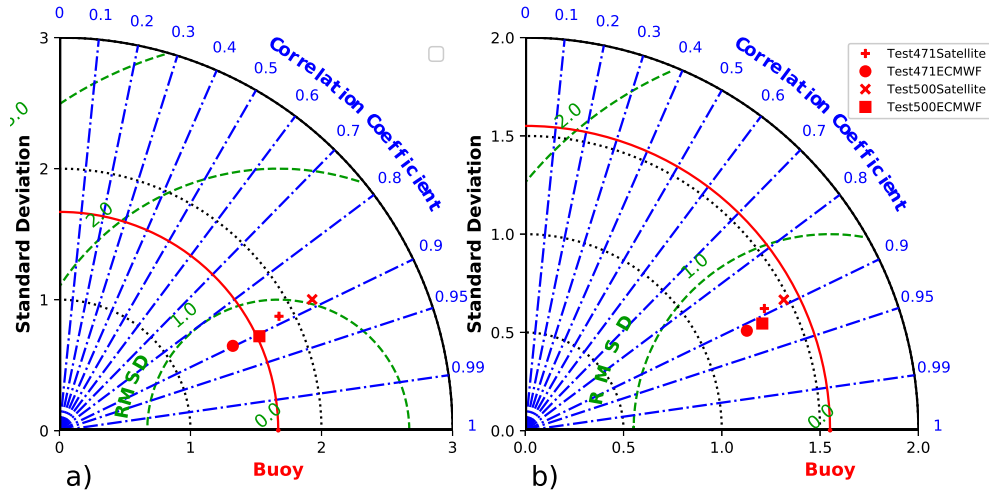


Figure 9: Taylor diagrams of significant wave height during storms in deep (a) and coastal (b) water.

449 ysis of storms occurred in the winter 2013/2014 at those locations. An ex-
 450 ample of spectral evolution during a storm is displayed in Figures 12 and 13
 451 for storm S10 at the coastal buoy 62069. At the beginning of the storm, the
 452 measured spectrum shows a variegated shape with multiple peaks (see for
 453 instance the secondary peak at 0.17 Hz and 200°) that are less marked in the
 454 modelled spectrum (T471ECMWF). At the end of the storm, the computed
 455 spectrum reproduces the secondary peak at frequencies lower than 0.1 Hz
 456 and direction nearly opposite with respect to mean storm direction, proba-
 457 bly due to wave reflection at the shoreline. Figure 13 highlights as the wide
 458 1-D frequency spectrum observed at the beginning of the storm tends to a
 459 more narrow shape as the storm attenuates towards the end. At the peak of
 460 the storm, the energy gap between the modelled spectra and the measured
 461 one is particularly evident. At the storm beginning, both the atmospheric
 462 S_{in} and the energy dissipation S_{ds} source terms proceeding from datasets us-
 463 ing satellite forcing are larger than those of the ECMWF dataset. Moreover,
 464 Test500 seems to give a smoother dissipation spectrum. This is consistent
 465 with Leckler et al. (2013) and is likely due to the averaging over wave scales
 466 of equation (11). On the contrary, as a result of its dissipation rate that is
 467 local in frequency, Test471 gives a higher dissipation rate at the peak fre-

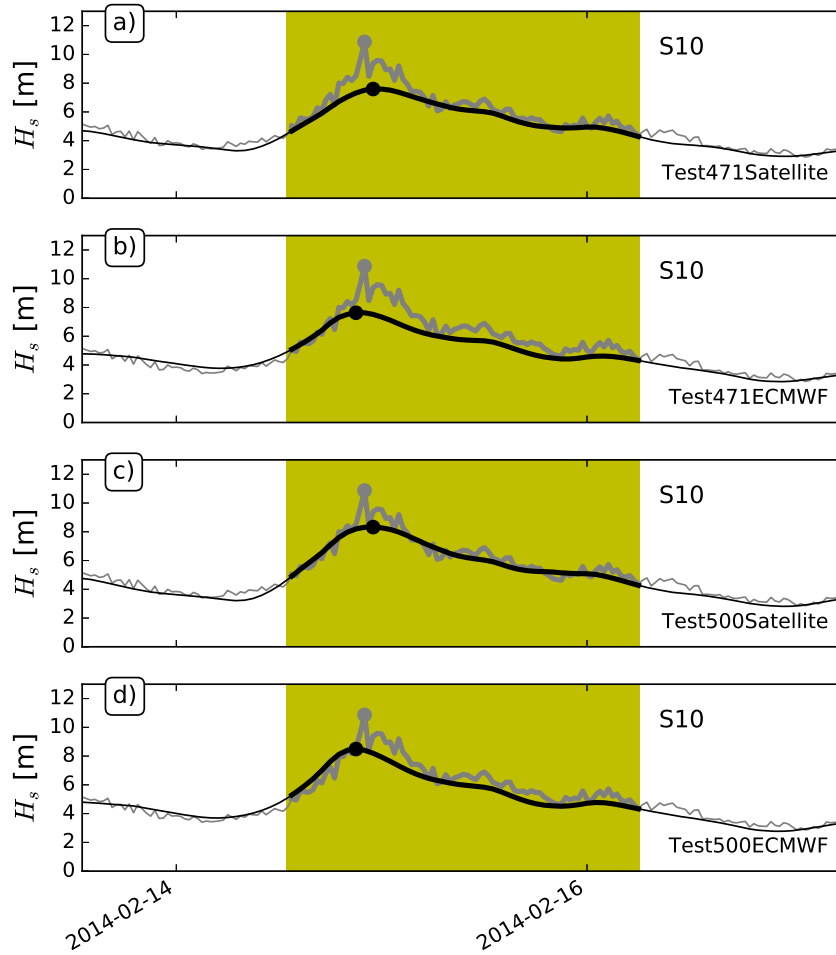


Figure 10: Observed (gray) and modelled (black) significant wave height H_s during storm S10 at buoy 5602. Thick lines highlights the H_s evolution during the storm. The circles indicate the extreme H_s values.

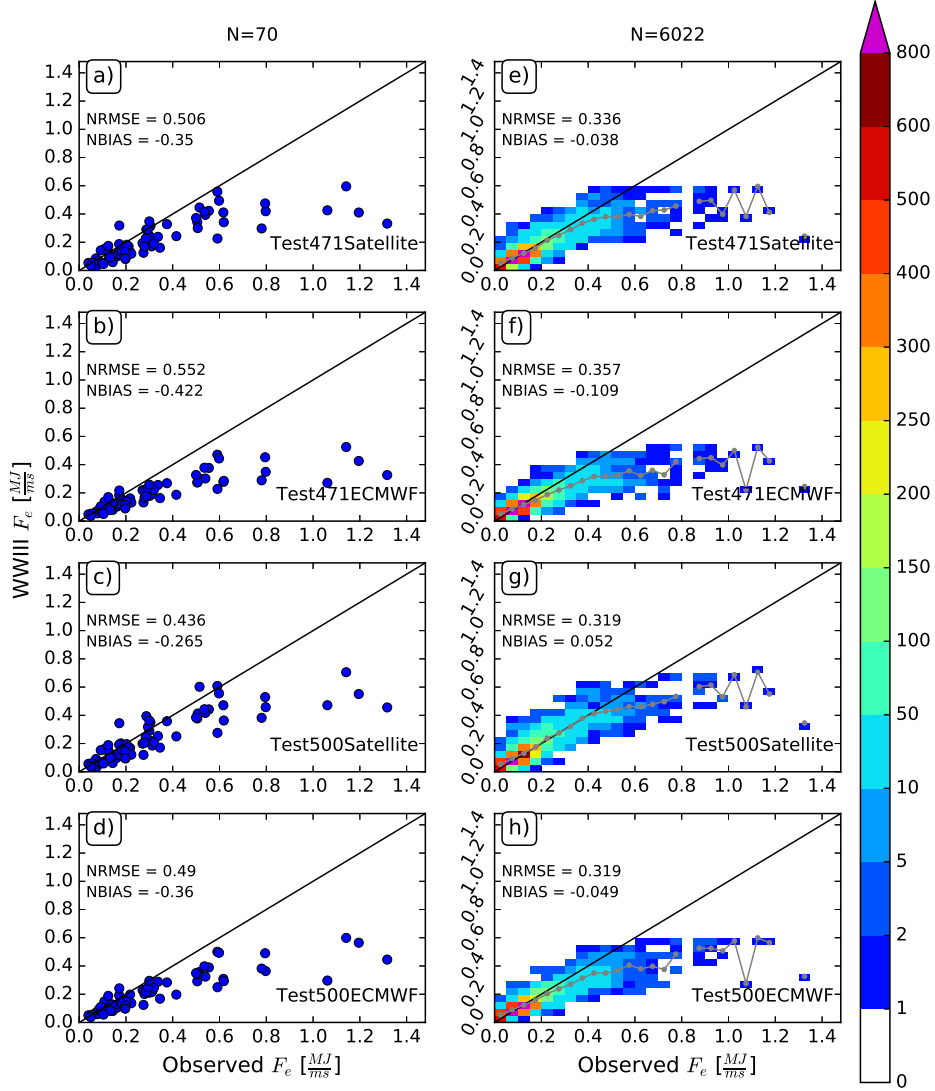


Figure 11: Scatter plot of observed versus modelled extreme (a-d) and collected during storms (e-h) energy flux F_e (a-d) in coastal water. The four datasets are shown. The grey line represents the mean of the model values.

468 quency at the beginning and at the peak of the storm. At the end of the
 469 storm, Test500 gives the higher dissipation rates. However, their impact on
 470 storm evolution seems to be limited since these dissipation rates at the end
 471 of the storm are three orders of magnitudes smaller than those at the storm
 472 peak.

473 The identification of the wind and swell components of the spectrum is
 474 carried out by means of the wave age criterion first introduced by Hanson
 475 and Phillips (2001). The wind sea component W is defined as:

$$476 \quad W = E^{-1}E|_{U_p > c}, \quad (17)$$

477 where E is the total spectral energy and $E|_{U_p > c}$ is the energy of the region
 478 of the spectrum under the direct influence of the wind. U_p is the projection
 479 of the wind speed, with direction θ , along the mean wave direction θ_w :

$$480 \quad U_p = CU_{10}\cos(\theta - \theta_w), \quad (18)$$

481 where C has been set equal to 1.7. Figure 14 shows the scatter plots of
 482 the wind and swell components of the significant wave height for the four
 483 datasets. Swell waves are characterized by a larger NRMSE than wind waves,
 484 with all the datasets that tend to underestimate extreme values larger than 6
 485 m. The extreme values of wind waves (> 10 m) are larger than those of swell
 486 waves. These extreme wind wave conditions are slightly underestimated, al-
 487 though the ECMWF forcing leads to a positive NBIAS due to overestimation
 488 of moderate values. Table 5 reports the error statistics of the sea and swell
 489 components of the four datasets at the coastal wave buoys. It is worth noting
 490 that all datasets have, respectively, positive and negative NBIAS for wind
 491 and swell waves under storm duration. Therefore, the virtually unbiased total
 492 H_s values during storms may be the result of a balance between a small over-
 493 estimation of the wind component combined with a small underestimation
 494 of the swell component.

495 *3.2. Storm tracking*

496 Figure 15 shows the result of the storm tracking process for storm S10.
 497 The storm path from its generation to its dissipation is superposed to the
 498 atmospheric pressure field at the time of storm arrival at buoy 62163 (see
 499 Figure 15b). The centre of the low pressure system lies few hundreds km
 500 west of the buoy. The large pressure gradients in the southern part of the

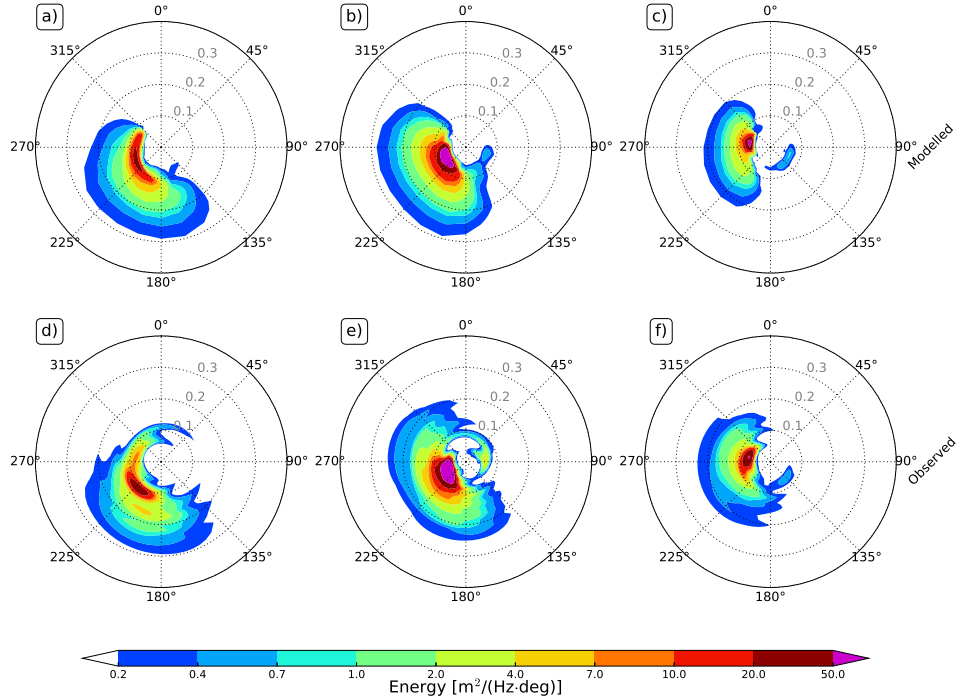


Figure 12: Computed (T471ECMWF) and measured frequency-directional wave spectra at the beginning (a and d), peak (b and e) and end (c and f) of the storm S10 at buoy 62069.

501 system are capable of driving strong westerly winds, as displayed in Figure
 502 16a.

503 The intense wind forcing in the southern part of the low pressure system
 504 controls the wave storm propagation across the Atlantic. Figure 16 high-
 505 lights the spatial relationship between the low pressure system and the wind
 506 and wave height fields as the storm hits the offshore buoy 62163. This Fig-
 507 ure displays the results obtained by the Test471ECMWF. The largest winds
 508 (in excess of 25 m/s) and significant wave heights (in excess of 10 m) are
 509 predicted to occur inside the half circle of 800 km radius depicted in Figure
 510 16.

511 To assess the model performance along the storm propagation, we retain
 512 the H_s altimeter measurements falling inside a half-circle of 800 km of radius

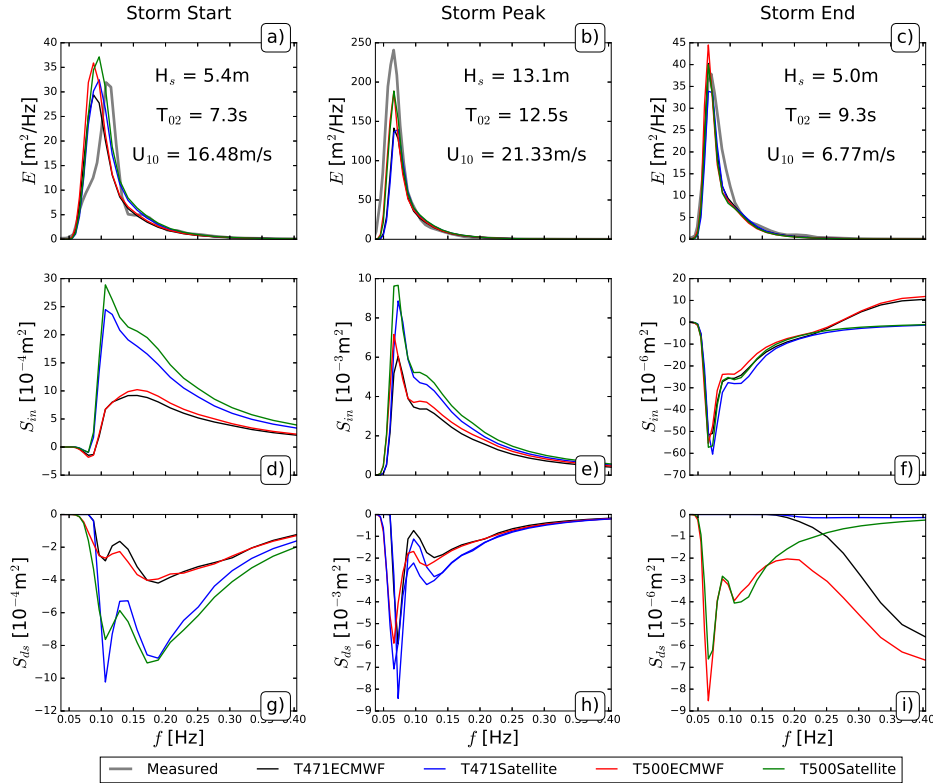


Figure 13: Frequency wave spectra at the beginning (a), peak (b) and end (c) of the storm S10 at buoy 62069 (T471ECMWF). The values of H_s and T_{02} are those measured by the buoy; the wind speed at 10 m U_{10} is from the ECMWF dataset. Atmospheric source terms (d-f). Dissipation source term (g-i).

513 south of the centre of the recognized low-pressure systems. See Figures 3
 514 and 16. Figure 17 shows the comparison between the H_s from altimeter
 515 measurements and from model computations along the storm propagation
 516 paths. The model results have been interpolated from the regular grid over
 517 the altimeter path. The observation of the scatterplots of Figure 17 draws the
 518 attention to the combined role played by model forcing and parameterization
 519 used. Whereas Test471Satellite and Test500ECMWF are characterized by
 520 minimal NBIAS values, Test500Satellite and Test471ECMWF give positive
 521 and negative NBIAS values, respectively. Test500ECMWF is the one showing
 522 the lowest NRMSE.

523 Figure 18 compares the wind from the ECMWF and satellite forcing

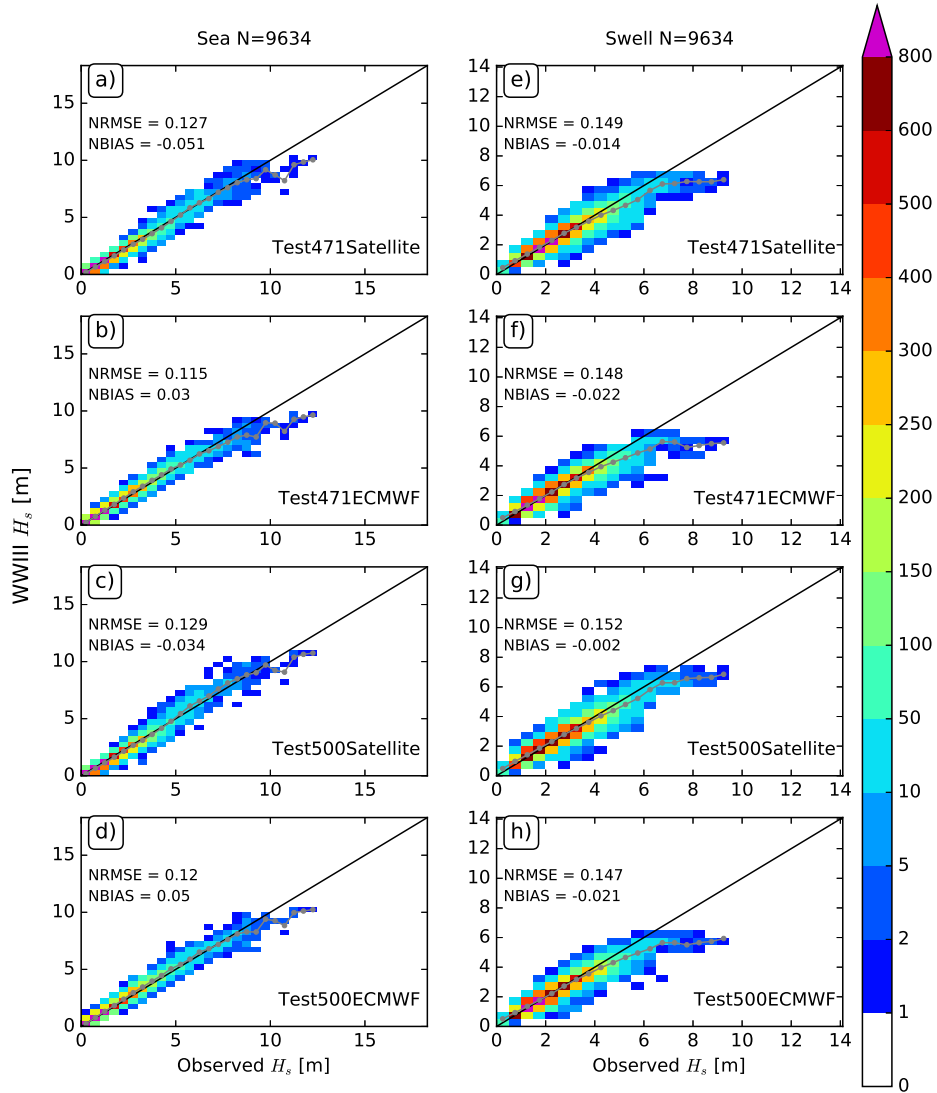


Figure 14: Scatter plot of observed versus modelled significant wave height H_s as the sea component (a-d) and the swell component (e-h). The four datasets are shown. The grey line represents the mean of the model values.

Table 5: Sea and swell waves statistics in coastal water.

H_s NRMSE						
Dataset	All	Extreme	Storm	All	Extreme	Storm
	Wind waves			Swell waves		
T471Satellite	0.13	0.13	0.11	0.15	0.14	0.11
T471ECMWF	0.12	0.14	0.10	0.15	0.15	0.11
T500Satellite	0.13	0.10	0.12	0.15	0.12	0.12
T500ECMWF	0.12	0.10	0.12	0.15	0.13	0.13
H_s NBIAS						
Dataset	All	Extreme	Storm	All	Extreme	Storm
	Wind waves			Swell waves		
T471Satellite	-0.05	-0.07	0.04	-0.01	-0.08	-0.08
T471ECMWF	0.03	-0.10	0.01	-0.02	-0.10	-0.07
T500Satellite	-0.03	-0.01	0.06	-0.00	-0.05	-0.04
T500ECMWF	0.05	-0.06	0.03	-0.02	-0.08	-0.04

524 datasets. The wind speed values are extracted along the low-pressure sys-
525 tems path propagation, thus corresponding to the time and location of H_s
526 values of figure 17. The NBIAS is slightly negative meaning that, along the
527 extra-tropical cyclone paths, the winds of ECMWF forcing are smaller than
528 those of the satellite forcing. This underestimation becomes more evident for
529 strong winds above 20 m/s. This is consistent with Figure 17, in which for a
530 given parameterization, NBIAS of H_s is lower with the adoption of ECMWF
531 forcing. In fact, the smaller ECMWF storm winds are likely to yield lower
532 energy transfer rates from the atmosphere to the wave motion, eventually
533 reducing the sea state growth along storm tracks.

534 4. Discussion

535 In this work, wave spectral numerical simulations under storm wave con-
536 ditions show a substantial dependence on the wind forcing and wave dissipa-
537 tion parameterization used. Roland and Ardhuin (2014) suggested that the
538 quality of wind data and source term parameterizations are the main factors
539 defining the accuracy of spectral wave results. Here, we address this subject

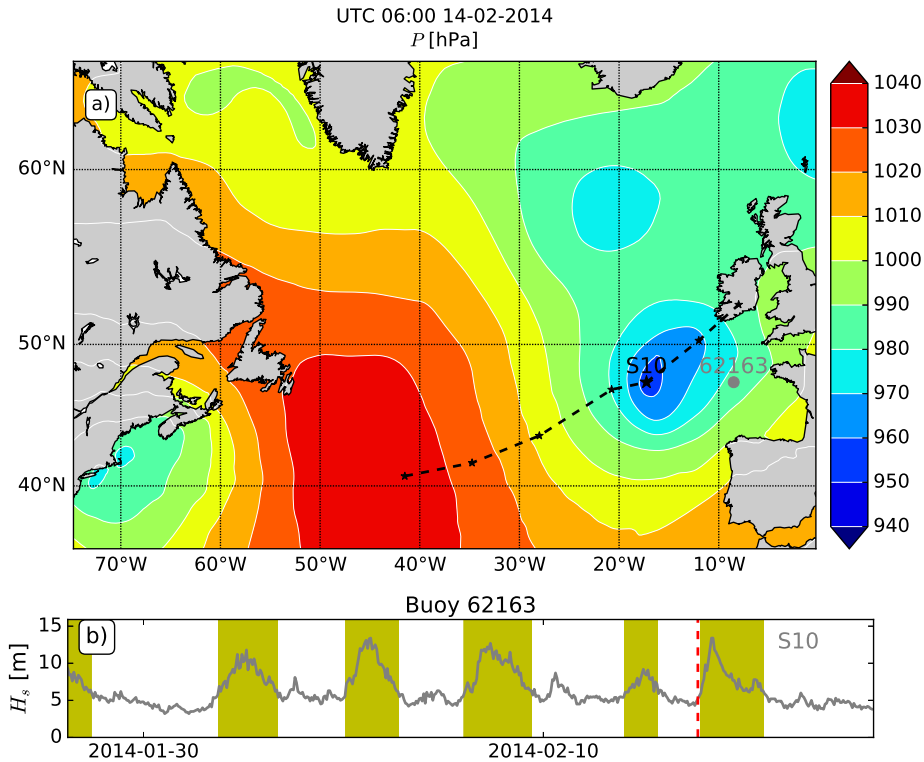


Figure 15: a) Atmospheric pressure field at the moment of the S10 storm arrival at the deep-water buoy 62163 (grey point). The dashed line indicates the low-pressure system path. b) Time series of significant wave height H_s recorded at the buoy 62163. The red dashed line marks the time instant of panel a). The storms at the buoy 62163 are highlighted in yellow.

540 under extreme storm conditions. This section highlights the main outcomes
 541 of the present study and discusses its results in the light of previous work.

542 A first analysis assesses the model performance separately at deep wa-
 543 ter buoys and coastal buoys. Model performance decreases when computed
 544 data are compared with buoy measurements in coastal water. This result is
 545 consistent with previous studies (Ravdas et al., 2018). In contrast with deep
 546 water waves, coastal waves are controlled by the combined effect of irregular
 547 shorelines, uneven bathymetry and mean water level oscillations. In addi-
 548 tion, the interaction with strong tidal currents is not negligible. Besides the
 549 challenges in modelling the complex physics of coastal wave processes, the

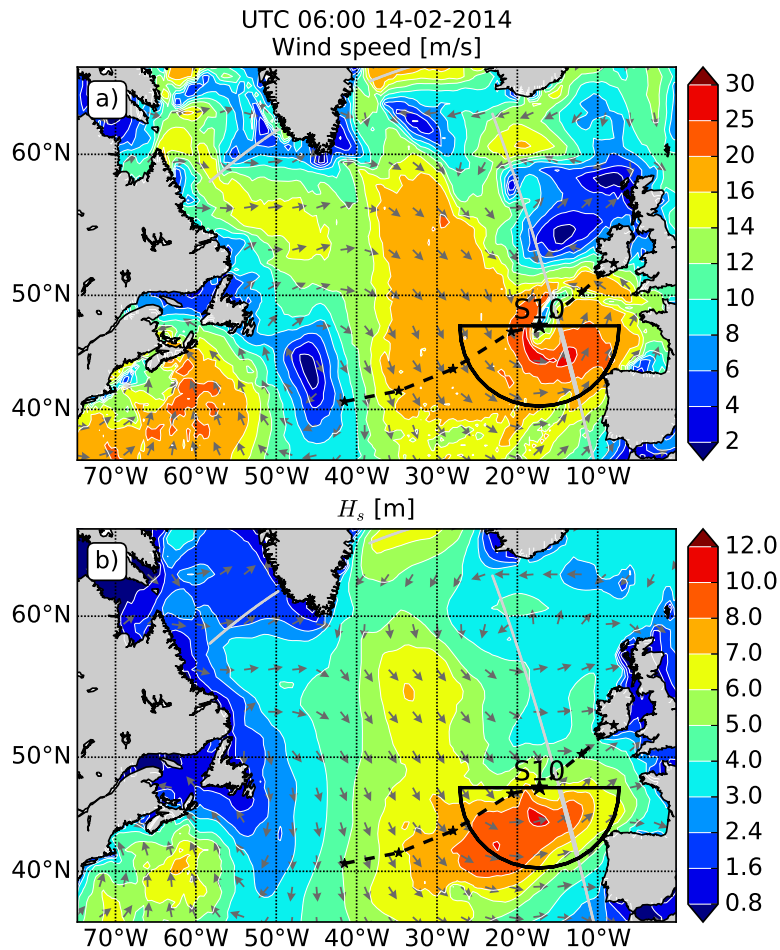


Figure 16: a) Wind speed field at the moment of the S10 storm arrival at the deep-water buoy 62163. b) Significant wave height H_s field at same time of panel a). The dashed line indicates the low-pressure system path. The solid black line shows the half circle with radius of 800 km. Altimeter measurement locations are shown by the grey dots.

550 quality of bathymetric and ocean circulation data play a significant role. In
 551 fact, tidal currents, mean water levels and bathymetry data are inevitably
 552 affected by errors that may propagate into the wave model and therefore
 553 decrease its accuracy in the nearshore.

554 The NRMSE and NBIAS values of H_s along storm tracks across the
 555 Atlantic are consistent with those at deep water buoys during storm duration.

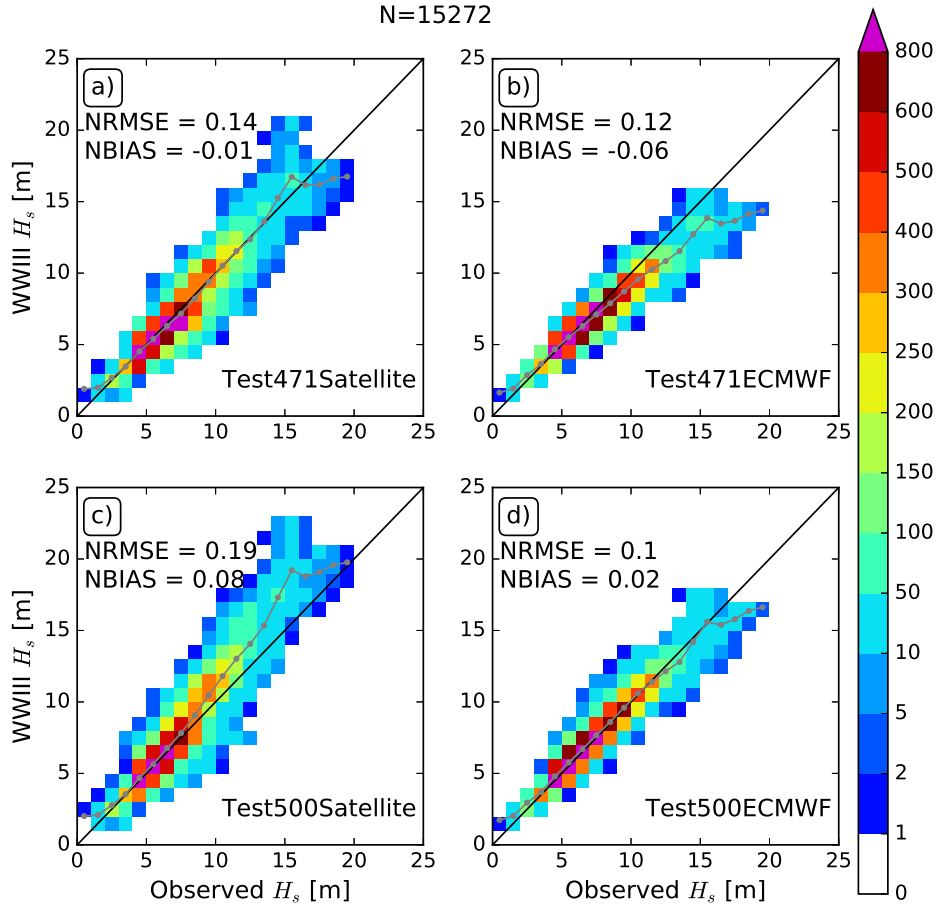


Figure 17: Scatterplots of the observed versus modelled significant wave height H_s along the storm tracks. Panels a), b), c) and d) show the comparison for different forcings and parameterizations. The grey line represents the mean of the model values.

556 For a given parameterization, the use of the wind forcing from satellite data
 557 tends to increase the NBIAS with respect to the use of the ECMWF wind
 558 forcing. This is likely to be related to an underestimation of extreme winds by
 559 the the ECMWF reanalysis dataset (Rasclé and Ardhuin, 2013), see Figure
 560 18. Analogously, for a given wind forcing, NBIAS rises when Test500 is used.
 561 This result is consistent with Filipot and Ardhuin (2012). In general terms,

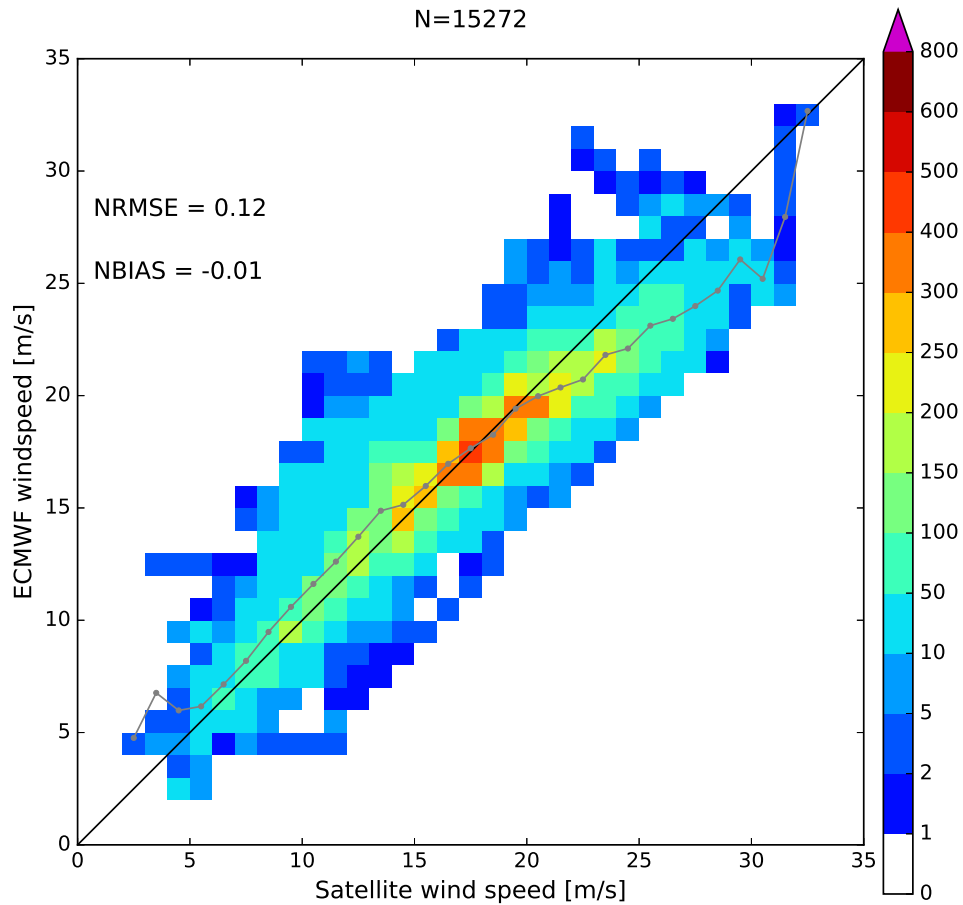


Figure 18: Scatterplot of satellite wind speed versus ECMWF wind speed along the storm tracks. The grey line represents the mean of the model values.

562 Test500ECMWF seems to be the most robust choice for the simulation of
 563 storm evolution both along storm tracks (NRMSE=0.1, NBIAS=0.02) and
 564 at buoy locations (NRMSE=0.1, NBIAS=-0.01).

565 The spectral analysis shows that all datasets tend to underestimate the
 566 swell component of H_s at four coastal buoys during storm conditions. Fig-
 567 ure 12 reveals that during an energetic storm a considerable amount of low-
 568 frequency energy is propagating with an opposite direction with respect to

569 the main storm direction. This highlights the importance of shallow water
570 processes, such as wave reflection at the shoreline, in determining the total
571 energy budget in coastal water. To have a first assessment of the impor-
572 tance of wave reflection during storms, we isolate the seaward component
573 of spectrum (retaining the seaward wave components that are more than
574 90° apart from the main wave direction). The comparison of the H_s with
575 the measurements shows that in the model this component is largely under-
576 estimated (with NBIAS ranging between -0.19 and -0.25 depending on the
577 dataset). Although the great part of wave energy is propagating shoreward,
578 this strong underestimation of the seaward component of the spectrum is
579 likely to contribute to the underestimation of the swell component under
580 storms in coastal water.

581 In contrast with its values during storm events, H_s at the storm peak
582 is systematically underestimated as revealed by its negative NBIAS values.
583 This result is valid at both offshore and coastal buoys. Although all datasets
584 share this trend, this underestimation is particularly marked using the combi-
585 nation of ECMWF forcing and Test471 parameterization: NBIAS=-0.15 and
586 -0.12 in deep and coastal water, respectively. The dataset Test500Satellite
587 provides the smallest NBIAS, in absolute values, thus reducing the under-
588 estimation. Although Test500Satellite provides the smallest NRMSE and
589 absolute NBIAS, it seems that it has the main drawback of overestimating
590 H_s larger than 15m (see Figures 7 and 17).

591 When comparing the results coming from the different model settings
592 described in this work, it is worth mentioning that the calibration of the two
593 wave breaking parameterizations used here has been carried out with the
594 ECMWF wind forcing (Tolman, 2016). Nevertheless, both parameterizations
595 perform well with satellite forcing showing minimal bias for the entire winter
596 timeseries. Since satellite data are expected to improve the characterization
597 of high wind conditions with respect to the ECMWF products (Bentamy
598 et al., 2017), we argue that a new calibration of parameterizations T471
599 and T500 with the satellite wind forcing may lead to an improvement of the
600 prediction of extreme sea states. However, the calibration task is beyond the
601 scope of this work, focusing on the winter 2013/2014, as longer simulations
602 are required.

603 Another aspect to be taken into account is that, as can be seen in Figure
604 10, H_s measurements are more noisy than simulated results. These spikes
605 are likely to enhance the H_s peak underestimation by the model that could
606 then be mitigated by applying a despiking filter to the measured timeseries.

607 However, we prefer to avoid this alteration due to its involved subjectivity.
608 It can be worth mentioning that Castelle et al. (2015) simply applied a linear
609 coefficient equal to 1.07 to adjust the H_s values from WWIII simulations to
610 the measurements from buoy 62064 under the same period.

611 An underestimation is found also for extreme mean wave period T_{02} and
612 energy flux F_e in coastal water. NBIAS for T_{02} is slightly smaller, in absolute
613 value, than that for H_s . On the other hand, the stronger underestimation of
614 peak values of F_e (NBIAS between -0.27 and -0.42) is due to the F_e parameter
615 definition, resulting from the product of E which is function of H_s^2 and c_g
616 which is function of wave period.

617 The observed underestimation of extreme wave parameters highlights the
618 importance of the choice of an accurate hindcast product for extreme wave
619 analysis purposes. In fact, long-term hindcasts affected by errors in extreme
620 sea state conditions can strongly impact the the probabilistic moments and
621 the tail of the distributions used for extreme event analysis (Campos et al.,
622 2019). This may have a crucial importance especially in calculation design.

623 *4.1. Impact of time resolution of forcing winds*

624 Due to the observed rapid evolution of sea states under extreme weather
625 conditions, it appears plausible that the time resolution of the wind forcing
626 might have an impact on wave model result accuracy. In this paper we have
627 tested two wind datasets with the same time resolution of 6 hours. Here,
628 we assess a possible negative impact of relatively low time resolutions of
629 the wind forcing dataset. The accuracy of the wave output proceeding from
630 simulations with the Test500 parameterization and forced by ECMWF ERA5
631 winds at one hour resolution is discussed.

632 In our case the high-resolution wind forcing does not lead to a reduction of
633 the NRMSE of H_s for the entire dataset in deep water (NRSME=0.10). The
634 H_s data stays unbiased (NBIAS<0.005). The main benefit of using a high-
635 resolution wind forcing seems to be related to the ability of catching extreme
636 H_s at the storm peak. In fact, the NRMSE for extreme H_s experiences a
637 small decrease (from 0.111 to 0.106). Moreover, the one hour time resolution
638 forcing leads to a smaller underestimation of extreme H_s : NBIAS passes
639 from -0.09 to -0.08. Although detectable, the impact of the time resolution
640 of the forcing winds is undoubtedly limited. The limited magnitude of this
641 improvement seems to be related to the lengthy evolution of Atlantic swells
642 that progressively gain energy along their tracks across the ocean. These
643 swells characterized by a large wave age are likely to dominate the sea state at

644 the considered wave buoys, thus reducing the impact of fast wind oscillations
645 included in a high time resolution wind forcing.

646 What we have observed here in terms of the impact of the increased time
647 resolution of winds on wave modelling is consistent with Mentaschi et al.
648 (2015) who suggested that a resolution increase of the forcing wind field (in
649 their case it was a spatial resolution increase) may not lead to an improve-
650 ment of single point statistics. According to previous studies (Cavaleri, 2009;
651 Ardhuin et al., 2007; Bertotti and Cavaleri, 2009) they attributed this result
652 to the so-called double penalty effect: some features and patterns may be
653 missed or reproduced in a wrong place in space and time by the model.

654 4.2. Parameterization ST6

655 Version 5.16 of WWIII includes the new package ST6 which is designed
656 for the parameterization of wind input, wave breaking and swell dissipation.
657 We comment here the results obtained by activating ST6. For our dataset,
658 setting the FAC parameter equal to 1.09, that means increasing the value of
659 the wind drag by 9%, yields a reduction of absolute NBIAS with respect to
660 the default value of FAC=1. This is in agreement with Zieger et al. (2015)
661 who used the same value in combination with CFSR wind reanalysis. In
662 fact, our results shows a clear under- and overestimation of H_s with the
663 other two values proposed by Zieger et al. (2015): FAC=1 in combination
664 with CFS winds and FAC=1.23 in combination with NOGAPS winds. A
665 more detailed sensitivity analysis of the FAC or other parameters included
666 in the parameterization ST6 is beyond the scope of this work.

667 Although the use of ST6 with FAC=1.09 leads to a small NBIAS for the
668 entire dataset (<0.04), H_s values at storm peaks remain underestimated.
669 With both Satellite and ECMWF wind forcing dataset, the use ST6 leads
670 to NBIAS values of extreme (at the storm peak) H_s comprised between the
671 values associated with Test471 and Test500. For instance, at deep water
672 buoys with ECMWF forcing, the NBIAS for extreme H_s is equal to -0.13, a
673 value that lies between the those associated with Test471 (-0.15) and Test500
674 (-0.09), see Table 3. This results suggest that, despite ineluctable differences,
675 the general behaviour of ST6 in predicting H_s under moderate and extreme
676 conditions is analogous to what we have already seen and commented for
677 Test471 and Test500 of the parameterization group ST4.

678 **5. Conclusions**

679 The aim of this work was to assess the impact of wave breaking parame-
680 terizations and wind forcing datasets on the accuracy of spectral wave model
681 results under storm wave conditions. We used the WWIII model to simulate
682 the storm sequence occurred in the winter 2013/2014 on the North-East At-
683 lantic. This work focused on two wave breaking parameterizations included
684 in the parameterization group ST4: Test471 and Test500. Moreover, we
685 tested two forcing datasets with six-hour time resolution winds: one based
686 on satellite observations and another based on the ECMWF ERA5 reanaly-
687 sis. The analysis was carried out firstly by identifying the individual storms
688 at North-East Atlantic buoy locations and then following the storm tracks
689 across the ocean. The main findings are summarized here:

- 690 1. The choice of the combination of the wave breaking parameterization
691 and the wind forcing dataset significantly affects the model results in
692 terms of NBIAS and NRMSE of wave parameters. This is valid for
693 wave parameters computed over the entire time series, during storm
694 evolution as well as at the storm peaks. The change of a given breaking
695 parameterization or wind forcing dataset leads to changes in NBIAS
696 and NRMSE of H_s and T_{02} that are on the order of 5%. Due to its
697 definition involving the product between group parameters function of
698 H_s^2 and T_{02} , F_e suffers more variability.
- 699 2. For a given wave dissipation parameterization and wind forcing, the
700 NBIAS and NRMSE values of H_s computed under storm conditions
701 at wave buoys are consistent with those computed along storm tracks
702 across the Atlantic. Test500 together with the satellite wind forcing
703 gives higher H_s values, thus increasing the NBIAS with respect to, re-
704 spectively, Test471 and ECMWF wind forcing. By improving the error
705 metrics, Test500ECMWF seems to represent the most robust choice for
706 simulating the storm evolution.
- 707 3. Negative NBIAS values of H_s at the storm peaks reveal a significant
708 underestimation of extreme wave conditions that is particularly marked
709 at the coastal buoy locations. This underestimation, common to all the
710 tested datasets, is reduced by using the Test500Satellite dataset.
- 711 4. The spectral analysis shows that at the coastal buoys a considerable
712 amount of energy is propagating seaward during storms, possibly as a
713 result of wave reflection at the shoreline. This seaward component is

714 strongly underestimated by the model (NBIAS of the order of -0.2),
715 thus contributing to the underestimation of the swell component at the
716 coastal buoy locations.

717 5. The use of the high-resolution wind forcing (one-hour resolution) ERA5
718 does not significantly improve the error statistics computed over the
719 entire time series at the wave buoys. The main benefit of using a
720 high-resolution forcing resides in the (limited, on the order of 1%) im-
721 provement of NRMSE and NBIAS values of extreme wave conditions
722 at storm peaks.

Acknowledgments

This work was financially supported by the ARCWIND project "Adap-
tation and implementation of floating wind energy conversion technology for
the Atlantic region" (EAPA 344/2016), which is co-financed by the European
Regional Development Fund through the Interreg Atlantic Area Programme.
Moreover, it benefited from government support managed by the Agence Na-
tionale de la Recherche under the program Investissement d'Avenir with the
reference ANR-10-IEED-0006-14 and ANR-10-IEED-0006-26 related to the
projects DiMe and CARAVELE.

References

- Ardhuin, F., Bertotti, L., Bidlot, J.R., Cavaleri, L., Filipetto, V., Lefevre, J.M., Wittmann, P., 2007. Comparison of wind and wave measurements and models in the western mediterranean sea. *Ocean Engineering* 34, 526 – 541. URL: <http://www.sciencedirect.com/science/article/pii/S0029801806001193>, doi:<https://doi.org/10.1016/j.oceaneng.2006.02.008>.
- Ardhuin, F., Marié, L., Rasclé, N., Forget, P., Roland, A., 2009. Observation and estimation of lagrangian, stokes, and eulerian currents induced by wind and waves at the sea surface. *Journal of Physical Oceanography* 39, 2820–2838. URL: <https://doi.org/10.1175/2009JP04169.1>, doi:10.1175/2009JPO4169.1, arXiv:<https://doi.org/10.1175/2009JP04169.1>.
- Ardhuin, F., Rogers, E., Babanin, A.V., Filipot, J.F., Magne, R., Roland, A., van der Westhuysen, A., Queffeuilou, P., Lefevre, J.M., Aouf, L., Collard, F., 2010. Semiempirical dissipation source functions for ocean waves. part

- i: Definition, calibration, and validation. *Journal of Physical Oceanography* 40, 1917–1941. URL: <https://doi.org/10.1175/2010JP04324.1>, doi:10.1175/2010JPO4324.1, arXiv:<https://doi.org/10.1175/2010JP04324.1>.
- Autret, R., Dodet, G., Fichaut, B., Suanez, S., David, L., Leckler, F., Ardhuin, F., Ammann, J., Grandjean, P., Allemand, P., Filipot, J.F., 2016. A comprehensive hydro-geomorphic study of cliff-top storm deposits on banneg island during winter 2013-2014. *Marine Geology* 382, 37 – 55. URL: <http://www.sciencedirect.com/science/article/pii/S0025322716302201>, doi:<https://doi.org/10.1016/j.margeo.2016.09.014>.
- Banner, M.L., Babanin, A.V., Young, I.R., 2000. Breaking probability for dominant waves on the sea surface. *Journal of Physical Oceanography* 30, 3145–3160. URL: [https://doi.org/10.1175/1520-0485\(2000\)030<3145:BPFDDO>2.0.CO;2](https://doi.org/10.1175/1520-0485(2000)030<3145:BPFDDO>2.0.CO;2), doi:10.1175/1520-0485(2000)030<3145:BPFDDO>2.0.CO;2, arXiv:[https://doi.org/10.1175/1520-0485\(2000\)030<3145:BPFDDO>2.0.CO;2](https://doi.org/10.1175/1520-0485(2000)030<3145:BPFDDO>2.0.CO;2).
- Bentamy, A., Grodsky, S.A., Elyouncha, A., Chapron, B., Desbiolles, F., 2017. Homogenization of scatterometer wind retrievals. *International Journal of Climatology* 37, 870–889. URL: <https://rmets.onlinelibrary.wiley.com/doi/abs/10.1002/joc.4746>, doi:10.1002/joc.4746, arXiv:<https://rmets.onlinelibrary.wiley.com/doi/pdf/10.1002/joc.4746>.
- Bentamy, A., Mouche, A., Grouazel, A., Moujane, A., Mohamed, A.A., 2019. Using sentinel-1a sar wind retrievals for enhancing scatterometer and radiometer regional wind analyses. *International Journal of Remote Sensing* 40, 1120–1147. URL: <https://doi.org/10.1080/01431161.2018.1524174>, doi:10.1080/01431161.2018.1524174, arXiv:<https://doi.org/10.1080/01431161.2018.1524174>.
- Bernier, N.B., Alves, J.H.G.M., Tolman, H., Chawla, A., Peel, S., Pouliot, B., Bélanger, J.M., Pellerin, P., Lépine, M., Roch, M., 2016. Operational wave prediction system at environment canada: Going global to improve regional forecast skill. *Weather and Forecasting* 31, 353–370. URL: <https://doi.org/10.1175/WAF-D-15-0087.1>, doi:10.1175/WAF-D-15-0087.1, arXiv:<https://doi.org/10.1175/WAF-D-15-0087.1>.
- Bertotti, L., Cavaleri, L., 2009. Wind and wave predictions in the adriatic sea. *Journal of Marine Systems* 78, S227 – S234. URL:

- <http://www.sciencedirect.com/science/article/pii/S0924796309001511>,
doi:<https://doi.org/10.1016/j.jmarsys.2009.01.018>. coastal Processes:
Challenges for Monitoring and Prediction.
- Besio, G., Mentaschi, L., Mazzino, A., 2016. Wave energy resource assessment in the mediterranean sea on the basis of a 35-year hindcast. *Energy* 94, 50 – 63. URL: <http://www.sciencedirect.com/science/article/pii/S0360544215014127>, doi:<https://doi.org/10.1016/j.energy.2015.10.044>.
- Biscara, L., Schmitt, T., Correard, S., Créach, R., 2014. Modèles numériques de bathymétrie pour la prévision hydrodynamique du dispositif vigilance vagues-submersions, in: *Journées Nationales Génie Côtier - Génie Civil*, pp. 547–556. doi:10.5150/jngcgc.2014.060.
- Boudiere, E., Maisondieu, C., Ardhuin, F., Accensi, M., Pineau-Guillou, L., Lepesqueur, J., 2013. A suitable metocean hindcast database for the design of marine energy converters. *International Journal of Marine Energy* 3-4, e40 – e52. URL: <http://www.sciencedirect.com/science/article/pii/S2214166913000362>, doi:<https://doi.org/10.1016/j.ijome.2013.11.010>. special Issue Selected Papers - EWTEC2013.
- Campos, R., Soares, C.G., Alves, J., Parente, C., Guimaraes, L., 2019. Regional long-term extreme wave analysis using hindcast data from the south atlantic ocean. *Ocean Engineering* 179, 202 – 212. URL: <http://www.sciencedirect.com/science/article/pii/S0029801818318110>, doi:<https://doi.org/10.1016/j.oceaneng.2019.03.023>.
- Castelle, B., Marieu, V., Bujan, S., Splinter, K.D., Robinet, A., Senechal, N., Ferreira, S., 2015. Impact of the winter 2013-2014 series of severe western europe storms on a double-barred sandy coast: Beach and dune erosion and megacusp embayments. *Geomorphology* 238, 135 – 148. URL: <http://www.sciencedirect.com/science/article/pii/S0169555X15001385>, doi:<https://doi.org/10.1016/j.geomorph.2015.03.006>.
- Cavaleri, L., 2009. Wave modeling—missing the peaks. *Journal of Physical Oceanography* 39, 2757–2778. URL: <https://doi.org/10.1175/2009JP04067.1>, doi:10.1175/2009JPO4067.1, arXiv:<https://doi.org/10.1175/2009JP04067.1>.

- Desbiolles, F., Bentamy, A., Blanke, B., Roy, C., Mestas-Nuñez, A.M., Grodsky, S.A., Herbette, S., Cambon, G., Maes, C., 2017. Two decades [1992-2012] of surface wind analyses based on satellite scatterometer observations. *Journal of Marine Systems* 168, 38 – 56. URL: <http://www.sciencedirect.com/science/article/pii/S0924796316302068>, doi:<https://doi.org/10.1016/j.jmarsys.2017.01.003>.
- Dodet, G., Bertin, X., Taborda, R., 2010. Wave climate variability in the North-East Atlantic Ocean over the last six decades. *Ocean Modelling* 31, 120 – 131. URL: <http://www.sciencedirect.com/science/article/pii/S1463500309002066>, doi:<https://doi.org/10.1016/j.ocemod.2009.10.010>.
- Filipot, J.F., Ardhuin, F., 2012. A unified spectral parameterization for wave breaking: From the deep ocean to the surf zone. *Journal of Geophysical Research: Oceans* 117. URL: <https://agupubs.onlinelibrary.wiley.com/doi/abs/10.1029/2011JC007784>, doi:10.1029/2011JC007784, arXiv:<https://agupubs.onlinelibrary.wiley.com/doi/pdf/10.1029/2011JC007784>.
- Filipot, J.F., Ardhuin, F., Babanin, A.V., 2010. A unified deep-to-shallow water wave-breaking probability parameterization. *Journal of Geophysical Research: Oceans* 115. URL: <https://agupubs.onlinelibrary.wiley.com/doi/abs/10.1029/2009JC005448>, doi:10.1029/2009JC005448, arXiv:<https://agupubs.onlinelibrary.wiley.com/doi/pdf/10.1029/2009JC005448>.
- Hanson, J.L., Phillips, O.M., 2001. Automated analysis of ocean surface directional wave spectra. *Journal of Atmospheric and Oceanic Technology* 18, 277–293. URL: [https://doi.org/10.1175/1520-0426\(2001\)018<0277:AAOOSD>2.0.CO;2](https://doi.org/10.1175/1520-0426(2001)018<0277:AAOOSD>2.0.CO;2), doi:10.1175/1520-0426(2001)018<0277:AAOOSD>2.0.CO;2, arXiv:[https://doi.org/10.1175/1520-0426\(2001\)018<0277:AAOOSD>2.0.CO;2](https://doi.org/10.1175/1520-0426(2001)018<0277:AAOOSD>2.0.CO;2).
- Hersbach, H., Bell, W., Berrisford, P., Horányi, A., J., M.S., Nicolas, J., Radu, R., Schepers, D., Simmons, A., Soci, C., Dee, D., 2019. Global reanalysis: goodbye ERA-Interim, hello ERA5 , 17–24 URL: <https://www.ecmwf.int/node/19027>, doi:10.21957/vf291hehd7.
- Holthuijsen, L.H., Powell, M.D., Pietrzak, J.D., 2012. Wind and waves in extreme hurricanes. *Journal of Geophysical Research: Oceans* 117. URL: <https://doi.org/10.1029/2011JC007784>.

- <https://agupubs.onlinelibrary.wiley.com/doi/abs/10.1029/2012JC007983>,
doi:10.1029/2012JC007983, arXiv:<https://agupubs.onlinelibrary.wiley.com/doi/pdf/10.1029/2012JC007983>
- Lazure, P., Dumas, F., 2008. An external-internal mode coupling for a 3D hydrodynamical model for applications at regional scale (MARS). *Advances in Water Resources* 31, 233 – 250. URL: <http://www.sciencedirect.com/science/article/pii/S0309170807001121>, doi:<https://doi.org/10.1016/j.advwatres.2007.06.010>.
- Leckler, F., Ardhuin, F., Filipot, J.F., Mironov, A., 2013. Dissipation source terms and whitecap statistics. *Ocean Modelling* 70, 62 – 74. URL: <http://www.sciencedirect.com/science/article/pii/S1463500313000474>, doi:<https://doi.org/10.1016/j.ocemod.2013.03.007>. *ocean Surface Waves*.
- Longuet-Higgins, M.S., 1952. On the statistical distribution of the heights of sea waves. *Journal of Marine Research* 11, 245–266.
- Masselink, G., Scott, T., Poate, T., Russell, P., Davidson, M., Conley, D., 2016. The extreme 2013/2014 winter storms: hydrodynamic forcing and coastal response along the southwest coast of england. *Earth Surface Processes and Landforms* 41, 378–391. URL: <https://onlinelibrary.wiley.com/doi/abs/10.1002/esp.3836>, doi:10.1002/esp.3836, arXiv:<https://onlinelibrary.wiley.com/doi/pdf/10.1002/esp.3836>
- Mathiesen, M., Goda, Y., Hawkes, P.J., Mansard, E., Martin, M.J., Peltier, E., Thompson, E.F., Vledder, G.V., 1994. Recommended practice for extreme wave analysis. *Journal of Hydraulic Research* 32, 803–814. URL: <https://doi.org/10.1080/00221689409498691>, doi:10.1080/00221689409498691, arXiv:<https://doi.org/10.1080/00221689409498691>.
- Mentaschi, L., Besio, G., Cassola, F., Mazzino, A., 2015. Performance evaluation of wavewatch iii in the mediterranean sea. *Ocean Modelling* 90, 82 – 94. URL: <http://www.sciencedirect.com/science/article/pii/S1463500315000578>, doi:<https://doi.org/10.1016/j.ocemod.2015.04.003>.
- Michaud, H., Dalphinnet, A., Huchet, M., Pasquet, A., Baraille, R., Leckler, F., Aouf, L., Roland, A., Sikiric, M., Ardhuin, F., Filipot, J.F., 2015. Implementation of the next french operational coastal wave forecasting

- system and application to a wave-current interaction study, in: 14th International Workshop on Wave Hindcasting and Forecasting and 5th Coastal Hazard Symposium.
- Miche, A., 1944. Mouvements ondulatoires de la mer en profondeur croissante ou décroissante. Forme limite de la houle lors de son déferlement. Application aux digues maritimes. Troisième partie. Forme et propriétés des houles limites lors du déferlement. Croissance des vitesses vers la rive. *Annales des Ponts et Chaussées Tome 114*, 369–406.
- Mironov, A.S., Dulov, V.A., 2007. Detection of wave breaking using sea surface video records. *Measurement Science and Technology* 19, 015405. doi:10.1088/0957-0233/19/1/015405.
- O'Reilly, W., Olfe, C.B., Thomas, J., Seymour, R., Guza, R., 2016. The california coastal wave monitoring and prediction system. *Coastal Engineering* 116, 118 – 132. URL: <http://www.sciencedirect.com/science/article/pii/S0378383916301120>, doi:<https://doi.org/10.1016/j.coastaleng.2016.06.005>.
- Perez, J., Menendez, M., Losada, I.J., 2017. Gow2: A global wave hindcast for coastal applications. *Coastal Engineering* 124, 1 – 11. URL: <http://www.sciencedirect.com/science/article/pii/S0378383917300443>, doi:<https://doi.org/10.1016/j.coastaleng.2017.03.005>.
- Phillips, O.M., 1984. On the response of short ocean wave components at a fixed wavenumber to ocean current variations. *Journal of Physical Oceanography* 14, 1425–1433. URL: [https://doi.org/10.1175/1520-0485\(1984\)014<1425:OTROSO>2.0.CO;2](https://doi.org/10.1175/1520-0485(1984)014<1425:OTROSO>2.0.CO;2), doi:10.1175/1520-0485(1984)014<1425:OTROSO>2.0.CO;2, arXiv:[https://doi.org/10.1175/1520-0485\(1984\)014<1425:OTROSO>2.0.CO;2](https://doi.org/10.1175/1520-0485(1984)014<1425:OTROSO>2.0.CO;2).
- Raschle, N., Ardhuin, F., 2013. A global wave parameter database for geophysical applications. part 2: Model validation with improved source term parameterization. *Ocean Modelling* 70, 174 – 188. URL: <http://www.sciencedirect.com/science/article/pii/S1463500312001709>, doi:<https://doi.org/10.1016/j.ocemod.2012.12.001>. ocean Surface Waves.
- Ravdas, M., Zacharioudaki, A., Korres, G., 2018. Implementation and validation of a new operational wave forecasting system of the

- mediterranean monitoring and forecasting centre in the framework of the copernicus marine environment monitoring service. *Natural Hazards and Earth System Sciences* 18, 2675–2695. URL: <https://www.nat-hazards-earth-syst-sci.net/18/2675/2018/>, doi:10.5194/nhess-18-2675-2018.
- Reguero, B.G., Losada, I.J., Méndez, F.J., 2018. A recent increase in global wave power as a consequence of oceanic warming, in: *Nature Communications*.
- Roland, A., 2009. Development of WWM II: Spectral wave modelling on unstructured meshes. Ph.D. thesis. Technische Universitat Darmstadt. 212 pp.
- Roland, A., Ardhuin, F., 2014. On the developments of spectral wave models: numerics and parameterizations for the coastal ocean. *Ocean Dynamics* 64, 833–846. URL: <https://doi.org/10.1007/s10236-014-0711-z>, doi:10.1007/s10236-014-0711-z.
- Ruju, A., Passarella, M., Trogu, D., Buosi, C., Ibba, A., De Muro, S., 2019. An operational wave system within the monitoring program of a mediterranean beach. *Journal of Marine Science and Engineering* 7. URL: <https://www.mdpi.com/2077-1312/7/2/32>, doi:10.3390/jmse7020032.
- Sandhya, K., Murty, P., Deshmukh, A.N., Nair, T.B., Shenoi, S., 2018. An operational wave forecasting system for the east coast of india. *Estuarine, Coastal and Shelf Science* 202, 114 – 124. URL: <http://www.sciencedirect.com/science/article/pii/S0272771417310417>, doi:<https://doi.org/10.1016/j.ecss.2017.12.010>.
- Scott, T., Masselink, G., O’Hare, T., Saulter, A., Poate, T., Russell, P., Davidson, M., Conley, D., 2016. The extreme 2013/2014 winter storms: Beach recovery along the southwest coast of england. *Marine Geology* 382, 224 – 241. URL: <http://www.sciencedirect.com/science/article/pii/S0025322716302766>, doi:<https://doi.org/10.1016/j.margeo.2016.10.011>.
- Simmons, A., Uppala, S., Dee, D., Kobayashi, S., 2007. Era-interim: New ecmwf reanalysis products from 1989 onwards , 25–35 URL: <https://www.ecmwf.int/node/17713>, doi:10.21957/pocnex23c6.

- Stopa, J.E., Ardhuin, F., Babanin, A., Zieger, S., 2016. Comparison and validation of physical wave parameterizations in spectral wave models. *Ocean Modelling* 103, 2 – 17. URL: <http://www.sciencedirect.com/science/article/pii/S1463500315001614>, doi:<https://doi.org/10.1016/j.ocemod.2015.09.003>. waves and coastal, regional and global processes.
- Thornton, E.B., Guza, R.T., 1983. Transformation of wave height distribution. *Journal of Geophysical Research: Oceans* 88, 5925–5938. URL: <https://agupubs.onlinelibrary.wiley.com/doi/abs/10.1029/JC088iC10p05925>, doi:[10.1029/JC088iC10p05925](https://doi.org/10.1029/JC088iC10p05925), arXiv:<https://agupubs.onlinelibrary.wiley.com/doi/pdf/>
- Tolman, H.L., 2016. User manual and system documentation of WAVEWATCH III version 5.16. Technical Report. NOAA/NWS/NCEP: 5830 University Research Court, College Park, MD 20740, USA.
- Tolman, H.L., Banner, M.L., Kaihatu, J.M., 2013. The nopp operational wave model improvement project. *Ocean Modelling* 70, 2 – 10. URL: <http://www.sciencedirect.com/science/article/pii/S1463500312001722>, doi:<https://doi.org/10.1016/j.ocemod.2012.11.011>. ocean Surface Waves.
- van Vledder, G.P., C. Hulst, S.T., McConochie, J.D., 2016. Source term balance in a severe storm in the southern north sea. *Ocean Dynamics* 66, 1681–1697. URL: <https://doi.org/10.1007/s10236-016-0998-z>, doi:[10.1007/s10236-016-0998-z](https://doi.org/10.1007/s10236-016-0998-z).
- Wadey, M.P., Haigh, I.D., Brown, J.M., 2014. A century of sea level data and the uk’s 2013/14 storm surges: an assessment of extremes and clustering using the newlyn tide gauge record. *Ocean Science* 10, 1031–1045. URL: <https://www.ocean-sci.net/10/1031/2014/>, doi:[10.5194/os-10-1031-2014](https://doi.org/10.5194/os-10-1031-2014).
- Young, I.R., Ribal, A., 2019. Multiplatform evaluation of global trends in wind speed and wave height. *Science* 364, 548–552. URL: <https://science.sciencemag.org/content/364/6440/548>, doi:[10.1126/science.aav9527](https://doi.org/10.1126/science.aav9527), arXiv:<https://science.sciencemag.org/content/364/6440/548>
- Zieger, S., Babanin, A.V., Rogers, W.E., Young, I.R., 2015. Observation-based source terms in the third-generation wave model wavewatch. *Ocean Modelling* 96, 2 – 25. URL:

<http://www.sciencedirect.com/science/article/pii/S1463500315001237>,
doi:<https://doi.org/10.1016/j.ocemod.2015.07.014>. waves and coastal, re-
gional and global processes.